NORTHWESTERN
UNIVERSITY

Center for Sustainable Engineering of Geological and Infrastructure Materials (SEGIM)

Department of Civil and Environmental Engineering

McCormick School of Engineering and Applied Science

Evanston, Illinois 60208, USA

Effect of Alkali Silica Reaction on the Mechanical Properties of Aging Mortar Bars: Experiments and Numerical Modeling

M. Pathirage, F. Bousikhane, M. D'Ambrosia,
M. Alnaggar and G. Cusatis

SEGIM INTERNAL REPORT No. 17-12/157E

Submitted to International Journal of Damage Mechanics *December 2017*

Journal Title
XX(X):2–32

DOI: 10.1177/ToBeAssigned
www.sagepub.com/
SAGE

Effect of Alkali Silica Reaction on the Mechanical Properties of Aging Mortar Bars: Experiments and Numerical Modeling

M. Pathirage[1], F. Bousikhane[1], M. D'Ambrosia[2], M. Alnaggar[3] and G. Cusatis[1]

Abstract

Alkali Silica Reaction (ASR) and its effect on concrete and mortar has been studied for many years. Several tests and procedures have been formulated to evaluate this reaction, particularly in terms of aggregate reactivity. However, the data given in the literature concerning the mechanical properties of concrete and mortar is scattered and very little information is available for some properties such as fracture energy. In this study, the mechanical behavior of mortar was evaluated and monitored, under normal and accelerated environmental conditions. Fracture energy, compressive strength and tensile strength were measured for mortar specimens, casted with highly reactive Spratt crushed aggregate, at two different storage temperatures (23°C and 80°C) and at two different alkali concentrations (immersed in water and in 1N NaOH solution). Moreover, free expansion tests (according to ASTM C1260) and petrographic observations were performed, in order to relate them to the evolution of the mechanical properties of mortar. Results show a decrease of the mechanical properties associated with specimens at 80°C in alkali solution and that the deterioration due to ASR is counter-balanced by the strengthening of mortar resulting from the hydration process. A multi-physics computational framework, based on the Lattice Discrete Particle Model (LDPM) is then proposed. Numerical simulations based on a complete calibration and validation with the obtained experimental data capture the behavior of mortar subjected to the complex coupled effect of strength build-up and ASR at different temperatures and alkali contents.

Keywords

Alkali Silica Reaction, Mortar, Aging, Cement Hydration, Mechanical Behavior, Modeling, Coupled Mechanism, Lattice Discrete Particle Model

Prepared using sagej.cls *[Version: 2015/06/09 v1.01]*

Introduction

For a long time, concrete has been used for the construction of infrastructures such as power plants, bridges and dams. Researchers and engineers have been interested in assessing durability and serviceability of such structures. One important issue they face is how to evaluate and monitor the changes of concrete mechanical properties due to deterioration over time as well as the induced consequences at the structural level. Alkali Silica Reaction is one of the many phenomena leading to deterioration of concrete structures. This reaction was first discovered by Stanton (1940) and consists of a chemical reaction between alkali hydroxides, mainly provided by cement, and silica contained in reactive aggregate. The reaction product is the so-called "ASR gel", which in high relative humidity environment adsorbs water, swells and generates internal pressure. Micro and macro-cracks may occur if this pressure is high enough in areas surrounding aggregate particles and within the aggregate itself.

Many aspects of ASR are still the subject of current research. These include the chemical composition of the gel (Lindgård et al., 2012; Louarn and Larive, 1993; Thaulow et al., 1996; Fernandes, 2009), its viscosity and the effect of calcium ions (Kawamura and Iwahori, 2004; Šachlová et al., 2010; Wang and Gillott, 1991a,b) and the controversial idea of gel flow (Moon et al., 2014). The chemical reaction associated with ASR has been studied for a long time: the hydroxyl ions first react with the silanol groups and then with the siloxane bridges, which leads to the dissolution of amorphous or poorly crystalline silica (Saouma and Hariri-Ardebili, 2014; Glasser and Kataoka, 1981; Wilson et al., 1994; Jensen et al., 1982; Chatterji et al., 1987; Dron and Brivot, 1992; Prince and Perami, 1993; Pan et al., 2012). The dissolved silica reacts with the calcium ions coming from $Ca(OH)_2$ and this stable reaction produces the tobermorite-type C-S-H. The reaction continues until $Ca(OH)_2$ is all consumed (Kim and Olek, 2014). Simultaneously, in order to maintain the electroneutrality, sodium and potassium ions Na^+ and K^+ are released from the cement paste (Glasser, 1979), which are then absorbed to create a highly polymerized, high alkali and low calcium hydrates [C-(Na/K)-S-H]: the alkali silica reaction gel (Dron and Brivot, 1993; Diamond, 2000).

Swelling and expansion of the ASR gel occur when the gel is in contact with water, which induces internal pressure. The mechanism is not fully understood and several theories exist to describe it. One explanation is the idea of osmotic pressure (Poole, 1992) generated by the cement paste and acting like a semi-permeable membrane. Water from the pore solution can pass through the cement paste but alkali and silica ions cannot. Other studies proposes that the dissolved silica diffuses away from the reactive aggregate particles, and this implies further expansion and swelling of the gel (Dron and Brivot, 1993). Another explanation is based on the electrical diffuse double layer theory proposed by Prezzi et al. (1997). A more convincing theory proposes that the swelling pressure is accumulated in the interfacial transition

[1]Department of Civil and Environmental Engineering, Northwestern University, Evanston, IL 60208, USA
[2]Materials & Mechanics, CTLGroup, Skokie, IL 60077, USA
[3]Rensselaer Polytechnic Institute, Troy, NY, USA

Corresponding author:
Gianluca Cusatis, Department of Civil and Environmental Engineering, Northwestern University, Evanston, IL 60208, USA
Email: g-cusatis@northwestern.edu

Prepared using sagej.cls

zone between aggregate and surrounding cement paste, because of water absorption (Bažant and Steffens, 2000).

If the internal pressure is high enough, micro-cracks occur and a typical crack pattern is a three-armed crack mapping (Sanchez et al., 2015). Other petrographic observations show not only micro-cracks at the interface between aggregate and cement paste, but also through the cement paste near large aggregate particles (Ben Haha, 2006; Ponce and Batic, 2006; Thomas et al., 2013). A process in five steps of the micro-structural changes due to ASR was proposed based on petrographic analysis by Katayama (2012) and Saouma et al. (2015): 1) formation of reaction rims, 2) exudation of gel on the reacted aggregate that partially fills microporosity in cement paste, 3) cracking through aggregates that are filled by gel, 4) gel formation in cracks from aggregates to cement paste and 5) gel precipitation (densification) in voids along cracks farther from aggregates.

Many key parameters affect the alkali silica reaction. The main ones are temperature, moisture content, alkali content, calcium content, silica content in aggregate, aggregate size and shape, porosity, and applied mechanical stress.

It is well-known that ASR is accelerated when temperature increases (Jensen et al., 1982; Swamy and Al-Asali, 1986; Jones, 1988; Larive, 1997) and it requires high humidity (80% or above) to occur (Chatterji et al., 1986; Olafsson, 1986). It is also important to note that at a higher curing temperature (from 50°C to 80°C) in humid conditions, one can observe an acceleration of the early strength development which however leads to a lower asymptotic value (Cebeci et al., 1989; Mirza et al., 1991). This leads to different ASR-induced damage evolution at high temperature. Moreover, high temperature relative to room temperature engenders a thermal expansion (Cruz and Gillen, 1980; Saccani et al., 2001) which must be dissociated from any expansion due to ASR.

As far as the alkali content is concerned, two categories can be distinguished: the alkali content provided by cement and the one from external sources. For both cases, the reaction is accelerated and the measurement of free expansion shows higher values when the alkali content is higher (Kawamura et al., 1988; Sibbick and Page, 1992; Smaoui et al., 2005). Several studies also show that in very high alkali contents, the gel structure changes and loses its swelling capability (Kagimoto et al., 2014).

This is the reason why many standard tests prescribe a higher curing temperature and a specific alkali content to determine if an aggregate type in a given concrete/mortar mix is deleterious. Indeed, the objective is to accelerate the ASR kinetics and thus get faster test results. For the aforementioned reasons, ASTM-C1260-07 (2007) is adopted in the present work for the experimental program.

The main consequence of ASR is finally the change in time of the mechanical properties of concrete/mortar. Many researchers have studied this issue, performing experimental work in the laboratory, as well as carrying evaluations from cores taken out from existing structures. It is generally agreed that ASR generates a significant decrease in Poisson's ratio, elastic modulus and tensile properties whereas compressive strength has more variability in its evolution (Ben Haha, 2006; Swamy and Al-Asali, 1986; Larive, 1997; Clark, 1990; Ono, 1990; Monette et al., 2000; Multon, 2003; Marzouk and Langdon, 2003; Na et al., 2016; Giaccio et al., 2008). The information available in the literature is scattered with reference to the evolution of the fracture energy.

Various models simulating Alkali Silica Reaction at different length scales exist in the literature, reflecting the multiscale nature of the problem. Early models considered an imposed volumetric expansion at the macroscopic scale, by using finite element modeling and treating ASR expansion as equivalent to an expansion due to thermal strain (Charlwood , 1994; Thompson et al., 1994; Léger

et al., 1996; Malla and Wieland, 1999). These models include the effect of temperature, moisture, alkali content and stress changes, which are, however, not related to the actual chemo-physical phenomena underlying ASR. These approaches are mostly based on phenomenological laws, which limits their range of application. Later on, chemo-mechanical models were proposed (Ulm et al., 2000; Li and Coussy, 2002; Capra and Sellier, 2003; Pignatelli et al., 2013), where reaction kinetics were taken in account as function of the temperature and humidity. Farage et al. (2004) and Fairbairn et al. (2004) used the model of Ulm et al. (2000) within a smeared crack plastic constitutive law. The external effect of mechanical loading on ASR and its consequences on the properties of concrete were then studied by using damage models (Capra and Sellier, 2003; Saouma and Perotti, 2006; Comi et al., 2009; Winnicki and Pietruszczak, 2008; Winnicki et al., 2014) and more complex damage coupled with hygro-thermo-chemical formulations (Bangert et al., 2004; Pesavento et al., 2012). At the aggregate level, within a predefined Representative Volume Element (RVE), mathematical models based on fracture mechanics were proposed by Bažant and Steffens (2000), whereas poro-mechanics models were formulated by Dormieux et al. (2004), Lemarchand et al. (2005), Bažant and Rahimi-Aghdam (2016) and Rahimi-Aghdam et al. (2016). Wu et al. (2014) proposed to simulate concrete as a multi-phase material and validated the model using a numerical homogenization scheme. Comby-Peyrot et al. (2009) modeled concrete as particles representing the aggregate and simulated ASR considering the swelling of the rim reaction gel product. In all the listed models, however, the results obtained for the physical crack distribution are typically limited: the work of Grimal et al. (2010) allowed ASR and anisotropic damage modeling using finite element method and was able to describe cracks and crack orientations by means of damage field plots. It is also worth mentioning the work of Bažant and Rahimi-Aghdam (2016) and Rahimi-Aghdam et al. (2016) that showed realistic crack patterns with the use of the microplane model and by simulating the fracture mechanics aspect using the crack band model. Alnaggar et al. (2013) proposed to overcome the lack of accurate crack simulation by considering ASR within a discrete model, the so-called Lattice Discrete Particle Model (LDPM) (Cusatis et al., 2011a,b) which describes concrete at the coarse aggregate length scale. This model, presented later in this paper, simulates separately the expansion due to the gel swelling and the induced cracking (Alnaggar et al., 2013, 2015). Variable humidity and temperature within concrete can be simulated and the model was able to successfully replicate experimental data considering the coupling effect between shrinkage, thermal strain and creep (Alnaggar et al., 2017).

Concerning the modeling of concrete/mortar strength build-up at early ages, multiple models can be found in the literature. The models of Ulm and Coussy (1995) and De Schutter and Taerwe (1996) described the early age strength growth by direct relation to cement hydration. The effect of temperature was taken in account in the work of Cervera et al. (1999) and Cervera et al. (2000) who introduced an intermediate parameter, the so-called aging degree, relating compressive strength, tensile strength, and elastic modulus with cement hydration degree. Other models (Bernard et al., 2003) considered a multiscale approach to predict the macroscopic elasticity evolution in time from the behavior of the C-S-H gel at the nanoscale.

Hygro-thermo-chemo-mechanical models at the macroscopic scale have shown to be capable of predicting aging concrete (Gawin et al., 2006; Pan et al., 2017). For example, the work of Di Luzio and Cusatis (2009a), Di Luzio and Cusatis (2009b) and Di Luzio and Cusatis (2013) describes at any age the moisture transport and heat transfer by taking in account chemical phenomena such as cement hydration, silica fume reaction and silicate polymerization through a Hygro-Thermo-Chemical (HTC)

model. This model was also successfully coupled with the LDPM framework and the two models were linked through the concept of aging degree by introducing aging laws relating cement hydration to the change in time of the mechanical parameters governing LDPM (Wan et al., 2016; Wendner et al., 2016).

The study presented in this paper overcomes the lack of models able to simulate the evolution of the mechanical properties of ASR affected mortar and the coupled effect of ASR deterioration and concrete/mortar aging. By conducting an experimental and a numerical program, this research aims to study aging mortar bars affected by ASR and conditioned according to ASTM C1260. Indeed, concrete and mortar aging plays a crucial role at early ages, when strength and other mechanical properties are expected to increase due to cement hydration The measurement of free expansion from the ASTM C1260 depends not only on the aggregate reactivity but also on the strength build-up that counterbalances the expansive nature of ASR. It is worth pointing out that the intertwined effect of ASR and aging has been observed qualitatively in the literature, however neither a systematic experimental work nor a comprehensive numerical coupling between damage due to ASR and aging formulations were ever performed.

Experimental Program

Materials and mixture proportions

For the mortar mix design, Spratt limestone was ordered from the Ministry of Transportation of Ontario, Canada. Spratt aggregate contains quartz, clay minerals and albite feldspar, in 40 wt.%, 54 wt.% and 6 wt.%, respectively, (Grattan-Bellew et al., 2010). This siliceous limestone incorporates chalcedony inclusions, it is highly reactive, and contains about 9% of silica. The aggregate was crushed and carefully washed, dried for 24 hours in oven at 105°C to remove any moisture content (Figure 1a). Then, the aggregate was sieved in accordance to ASTM C1260 (Figure 1b) and stored in separated and sealed boxes (Figure 1c). Table 1 shows the aggregate sieve size and proportions. Mortar bars were cast with the mix design reported in Table 2 in batches of three bars of size 254 mm $\times$ 25.4 mm $\times$ 25.4 mm, before being covered and placed in the curing room at controlled room temperature 23°C and 100% humidity for 24 hours (Figure 1d-e-f). A slight amount of lubricant WD-40 was sprayed on the molds to prevent any damage on the samples during demolding. The cement used was QUIKRETE Portland Cement

Table 1. Aggregate sieve size and proportions according to ASTM C1260.

Sieve Size	% Mass Retain	% Cum Retain	% Passing
#4 (4.75 mm)	0.0	0.0	100
#8 (2.36 mm)	10.0	10.0	90.0
#16 (1.18 mm)	25.0	35.0	65.0
#30 (0.60 mm)	25.0	60.0	40.0
#50 (0.30 mm)	25.0	85.0	15.0
#100 (0.15 mm)	15.0	100	0.0

Commercial Grade Type I/II, which complies with ASTM C150, as required by ASTM C1260. Lumps were removed by passing the cement through a #20 (0.85 mm) sieve.

The water used in the mix came from tap water, and was stored for several days before mixing in order to be at room temperature.

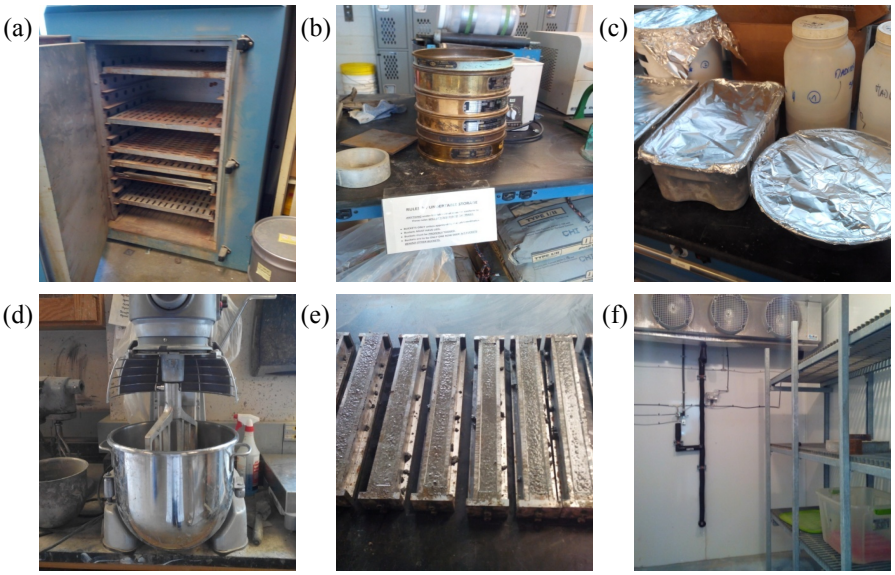

Figure 1. (a) Oven to dry the aggregate, (b) Aggregate sieving, (c) Sealed storage boxes, (d) Mortar mixer, (e) Casted mortar bars, (f) Curing room: 23°C at 100% humidity for 24 hours.

Table 2. Mixture proportions according to ASTM C1260 for the preparation of three mortar bars of size 254 mm × 25.4 mm × 25.4 mm.

Mortar	For three samples
Water to cement ratio	0.47
Water	206.8 g
Cement	440 g
Crushed Aggregates	990 g

Test program and details

The test program consisted of four cases, corresponding to four different environmental conditions. The first two cases are designated as samples 23A and 23W. They define specimens immersed in 1N NaOH at 23°C and specimens immersed in water at 23°C respectively. The two remaining cases are called samples 80A and 80W, which define the specimens immersed in 1N NaOH at 80°C and the specimens immersed in water at 80°C respectively. After one day of curing, the mortar bars were demolded and placed in different storage conditions. Samples 23A and 23W were directly placed in water at 23°C for another 24 hours. Samples 80A and 80W were placed in a box containing water at 23°C. This box was sealed and placed in a water bath at 80°C for another 24 hours. This procedure allowed avoiding thermal shock and potential micro-cracks. Finally, after the duration of 24 hours, samples 23A were placed in a solution of 1N NaOH at 23°C, samples 23W were kept in water 23°C, samples 80A were placed in a solution of 1N NaOH at 80°C and samples 80W were kept in water at 80°C. The temperature and alkali content were monitored and kept constant by using infrared temperature sensor and by controlling the pH and water level in the solutions.

Immediately after demolding and prior to the placement in water, the mortar bars were cut into different sizes according to each mechanical tests specifications. Free expansion were measured, along with petrographic observations to evaluate the ASR reactivity in the four cases. Semi-adiabatic calorimetric tests were performed in order to characterize the cement hydration signature. Subsequently, uniaxial unconfined compression, notched three point bending and Brazilian tests were performed at two different ages: 6 and 16 days after casting.

Free expansion measurements were performed in accordance to ASTM C1260 and ASTM C490 (Figure 2a), at different ages up to 16 days after casting. The dimensions of the sample were 254 mm $\times$ 25.4 mm $\times$ 25.4 mm. A Humboldt length comparator was used to measure expansions with an accuracy of 0.00254 mm. Petrographic analysis were done at CTLGroup, using stereo-optical microscopy on

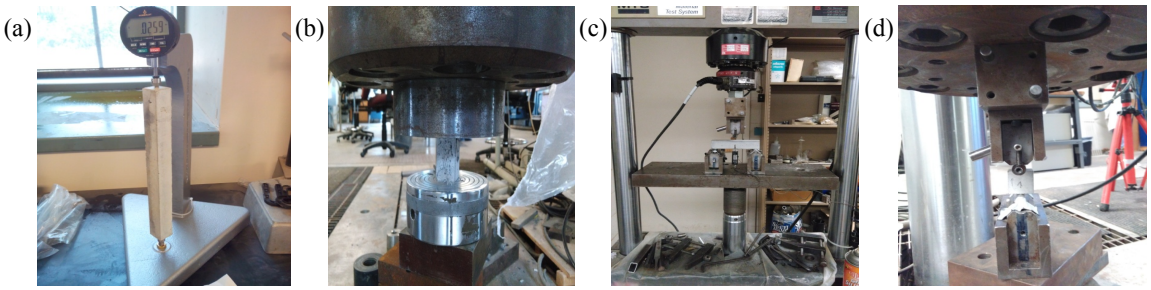

Figure 2. (a) Free expansion measurements, (b) Uniaxial unconfined compression test, (c) Notched three point bending test, (d) Brazilian test.

polished cross-sections at age 6 and 16. The samples underwent multiple processes of grinding and lapping, i.e. three grinding steps using a grinding wheel and diamond grinding disks of size 60, 30 and 12 micrometers, until reaching a smooth, lapped surface to perform the petrography.

Semi-adiabatic calorimetric tests were performed on three specimens. Figure 7a shows the used setup. For each test, mortar was casted into a cylinder of size 50.8 mm $\times$ 203.2 mm (diameter$\times$height) which was placed in the calorimeter right after casting, along with a thermocouple placed at the center of the cylinder to keep track of the evolution in time of the temperature. The measurements were recorded for 4 days at 1 minute intervals.

Uniaxial unconfined compression tests were performed on mortar prisms of size 50.8 mm $\times$ 25.4 mm $\times$ 25.4 mm, at age 6 and 16, under displacement control, with a loading rate of 0.003 mm/s (Figure 2b). The analysis of the load displacement curve provides the compressive strength $f_c^{'}$.

Three point bending tests on notched beams were also conducted at age 6 and 16 (Figure 2c). The dimensions of the beams were 127 mm $\times$ 25.4 mm $\times$ 25.4 mm, with a single edge notch of length $a_0 = 12.7$ mm and width 2.54 mm. The span was $S = 101.6$ mm. The test was performed under crack mouth opening displacement (CMOD) control via an extensometer attached to both sides of the notch, and with a loading rate of 0.003 mm/s. The load-displacement curve provides the peak force P_f before softening and the work of fracture W_F, which is the area under the curve. One can then estimate the energy required to create an unit area of crack:

$$G_F = \frac{W_f}{b(D - a_0)} \tag{1}$$

where G_F is the fracture energy, $b(D - a_0)$ is the initial cross sectional area of the ligament, $b = 25.4$ mm and $D = 25.4$ mm are the thickness and the width of the specimen, respectively. Moreover, one can define and compute the nominal fracture stress, as Bažant and Planas (1997):

$$\sigma_n^f = \frac{3}{2}\frac{P_f S}{bD^2} \tag{2}$$

Finally, Brazilian tests on mortar cubes of size 25.4 mm $\times$ 25.4 mm $\times$ 25.4 mm were performed at age 6 and 16, under displacement control, with a loading rate of 0.003 mm/s (Figure 2d). One can estimate the tensile strength of mortar by deriving the state of stress when the applied load P_t reaches its maximum:

$$f_t = \frac{2P_t}{\pi L^2} \tag{3}$$

where $L = 25.4$ mm is the length of the cube.

For each test described, a set of 3 specimens were tested for a total of 84 samples and the average properties were extracted.

EXPERIMENTAL RESULTS

Free expansion

Figure 3a shows the free expansion curves for the four different cases. They were obtained by length change readings at each different ages, to the nearest 0.001%. The goal here was, along with petrography, to identify the non-reactive (reference) cases and the reactive cases.

Samples 23W did not exhibit expansion during the whole experiment duration. This result is predictable since the environmental factors accelerating ASR, namely the high temperature and the high alkali content solution were absent.

Also samples 23A did not show any expansion, even though the specimens were immersed in 1N NaOH solution. Indeed, the imposed room temperature was not high enough for the reaction to be accelerated and to develop during the 16 days of the tests.

Samples 80W had only a small increase in length of about 0.04% from age 2 days to age 3 days. This change in length is associated with thermal expansion. In order to corroborate this result, Figure 3a also shows thermal expansion of mortar made with Elgin sand exposed to a temperature of 80°C, with a similar water to cement ratio (Cruz and Gillen, 1980).

On the contrary, samples 80A exhibited significant expansion, as expected on a typical ASTM C1260 test of a highly reactive aggregate such as Spratt. One can observe the characteristic S-shape curve suggesting no or very little reaction happening at the beginning, followed by a high reaction rate which then decreases in time. A final expansion value of 0.375% was obtained at age 16 days, Previous studies on Spratt aggregate report a mean expansion of 0.389% after 16 days (Nixon et al., 2016). The final expansion is much larger than the threshold defined in ASTM C1260 of 0.1% confirming the high reactivity of Spratt aggregate.

Although samples 23W and 23A did not show expansion, and the slight increase of length for mortar 80W is only associated to thermal expansion, it is uncertain to conclude that ASR did not happen at all. Petrographic observations are needed to draw a reliable conclusion.

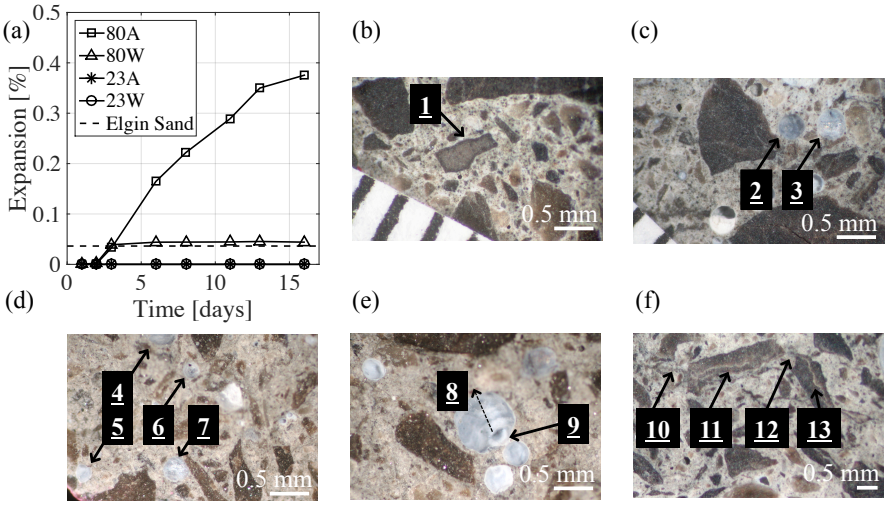

Figure 3. a) Free expansion evolution in time, b) Mortar 80A at age 6: reaction rim, c) Mortar 80A at age 6: gel-filled air voids at early stages, d) Mortar 80A at age 16: gel-filled air voids, e) Mortar 80A at age 16: multi-layer gel structure at later stages, f) Mortar 80A at age 16: gel-filled crack crossing multiple aggregate and cement paste.

Petrographic observation

Petrographic analyses were performed at age 6 and 16 for all four cases. No evidence of ASR, i.e. presence of alkali silica gel, was found in mortar 23W, 23A and 80W. This result corroborates the free expansion data. It would be appealing to use more sophisticated techniques to look into the micro-structural evolution in mortar. However, this was outside the scope of this study, since petrography was performed with the main objective of simply confirming the presence or absence of ASR gel in the different samples.

As expected, ASR gel was found in a large quantities in samples 80A. It is interesting to note that ASR gel was evenly distributed through the 25.4 mm $\times$ 25.4 mm square section, regardless of the distance from the edges.

This proves that the diffusion process of alkali ions from the external source to the inner part of mortar happened very fast (in only four days), due to the small sample dimensions. Another important factor is the use of crushed aggregates in the mix, which exposes the amorphous silica, thus increasing its overall specific surface. Figure 3b,c show polished cross-sections of mortar 80A at age 6. Aggregate pieces and cement paste are easily distinguishable.

The arrow n°1 shows what is frequently reported in the literature as a reaction rim. It is defined as a layer of alkali silica reaction product surrounding the reacted aggregate particle. Arrows n°2 and 3 show the presence of gel in air voids. The morphology and texture of the gel indicate that only a thin layer of gel is present. At age 6 days, only a few air voids were gel-filled which reveals that ASR was still at early stages. Interestingly, one can note that the two gel-filled voids are both next to aggregate particles. This observation tends to show that gel produced at the surface of aggregate migrates into adjacent voids. It would be compelling, although out of the scope of the present study, to relate the chemical composition of the gel to its flowability.

Figure 3d,e,f show polished sections of samples 80A at age 16 days. Arrows n°4 to 7 indicate air voids filled with gel. The number of gel-filled pores in the paste increased significantly from age 6 days to age 16 days, due to the high reaction rate also observable in the expansion curve (Figure 3a). One can observe that even though there is at least one adjacent aggregate next to most gel-filled air voids, some of them seem isolated. The hypothesis is that below these air voids, there is possibly a source of silica (aggregate) which is not observable in the section plane.

Arrows n°8 and 9 corroborate such a hypothesis: arrow n°9 points at a small dark area at the center of the pore, which appears to be the surface of an aggregate present below the observed section plane. Dashed arrow n°8 shows clearly multiple circular layers, emanating from the surface of the reacted aggregate, which then appear to fill progressively, layers by layers, the void upwards. The texture of the gel layers, their translucence and apparent larger thickness compared to the gel in n°3 void suggest that this multi-layer structure is a clear sign of an advanced reaction stage.

Finally, arrows n°11 and 13 show two aggregate particles in which gel-filled cracks go through. This phenomena is commonly observed in ASR affected concrete/mortar and demonstrates the important swelling pressure occurring in the internal mortar structure. It is interesting to note that the two aggregate particles are crossed by the same crack: indeed, the crack filled with gel goes from one aggregate to the other though the cement paste (arrows n°10 and 12).

These changes in the micro-structure due to ASR imply changes at the macro-scale level, in particular in terms of mechanical properties and behavior.

Calorimetric tests

Figure 4 shows the experimental data (average curve of three samples) obtained from the calorimetric tests. One can notice the typical shape of the curve describing temperature rise as a function of time. Four phases can be dissociated (Bullard et al., 2011): 1) rapid initial process that corresponds to the dissolution of cement constituents, 2) the dormant or induction period during which no reaction occurs, 3) the acceleration period as a consequence of C_3S hydration and 4) the deceleration period that is explained by the need for water to diffuse to the unreacted cement particles or for the dissolved ions from cement to diffuse outward into capillary pores.

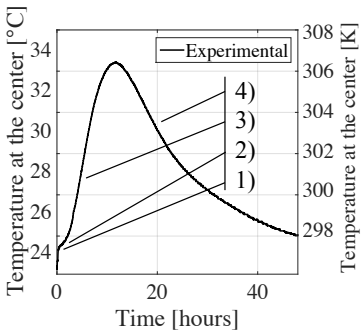

Figure 4. Four phases in the temperature rise curve from semi-adiabatic calorimetric tests

Mechanical behavior

Table 3 and Table 4 summarize the results from expansion measurements, compressive strength ($f_c^{'}$), fracture properties (G_F and σ_n^f) and indirect tensile test (f_t) strength, at two different ages and for the four different environmental conditions described earlier. The reported values are generated as the average of three tests. Figure 5 shows the evolution of the aforementioned mechanical properties in time.

Samples 23W exhibit, as a result of the aging process, an increase of compressive and tensile strength, and fracture properties from age 6 days to age 16 days. The same conclusion applies to samples 23A, which were identified to be ASR free. At age 6 days, samples 80W have higher values of compressive and tensile strength than samples 23W and 23W, however the fracture energy and nominal fracture stress are approximately the same for the three cases. At age 16 days, the compressive strength and the fracture energy of samples 80W are clearly below the ones of samples 23W and 23A. Finally, samples 80A show significant damage at early and late stages. The high expansion is well correlated with its mechanical behavior: at age 6 days, although it is not clear for fracture energy, there is a clear difference of compressive and tensile strength, and nominal fracture stress compared to samples 23W, 23A and 80W. At age 16 days, one can observe an increase of the mechanical properties, less pronounced for the fracture energy but significant for the tensile strength. The experimental work provided the confirmation that

Table 3. Experimental program results at 23°C.

Properties	23A		23W	
	6	16	6	16
ASR [Y/N]	No	No	No	No
Expansion [%]	0.000	0.000	0.000	0.000
$f_c^{'}$ [MPa]	30.33	40.12	29.84	42.03
G_F [N/m]	60.63	86.38	60.27	89.26
σ_n^f [MPa]	1.79	1.92	1.79	2.12
f_t [MPa]	1.80	2.83	2.00	3.13

Table 4. Experimental program results at 80°C.

Properties	80A		80W	
	6	16	6	16
ASR [Y/N]	Yes	Yes	No	No
Expansion [%]	0.165	0.375	0.044	0.044
$f_c^{'}$ [MPa]	26.32	27.91	32.76	34.33
G_F [N/m]	62.05	62.58	55.91	67.50
σ_n^f [MPa]	1.32	1.60	1.68	1.82
f_t [MPa]	1.57	2.33	2.13	2.75

there is indeed a decrease in the mechanical properties of mortar due to ASR. However the deterioration is counter-balanced by the strengthening resulting from the hydration process.

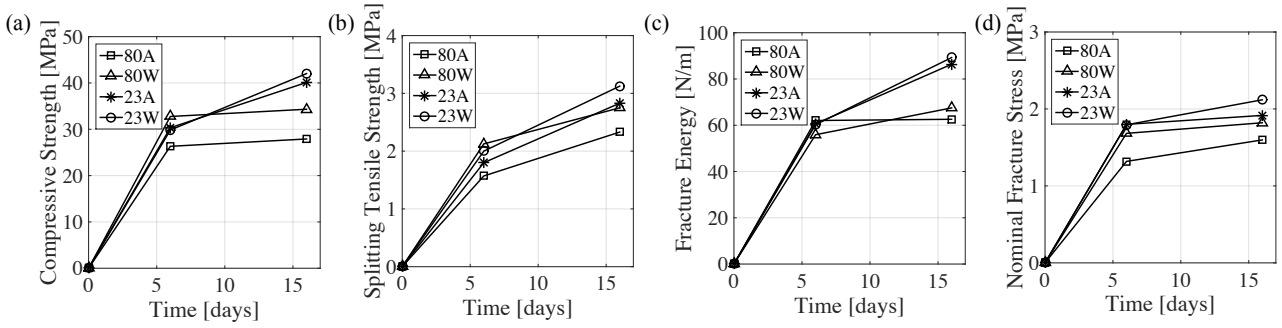

Figure 5. Variation in time of mechanical properties for the four different environmental conditions a) Compressive strength, b) Splitting tensile strength, c) Fracture strength, d) Nominal fracture stress.

COMPUTATIONAL PROGRAM

Overall framework

As described in the introduction, the simulation of hygro-thermo-chemo-mechanical coupling, as well as ASR damage, is performed within the Lattice Discrete Particle Model (LDPM) (Cusatis et al., 2011a,b) coupled with the Hygro-Thermo-Chemical (HTC) model (Di Luzio and Cusatis, 2009a,b, 2013), the aging model (Wan et al., 2016) and the ASR model (Alnaggar et al., 2013, 2015, 2017).

LDPM is a mesoscale model that simulates the interaction between aggregate particles contained in concrete/mortar (Schauffert et al., 2011a,b; Cusatis, 2013; Smith et al., 2014; Rezakhani and Cusatis, 2016; Ceccato et al., 2017). For a given volume of material, spherical particles are randomly placed from the largest to the smallest size using a trial and error procedure. The placement follows a particle size distribution curve consistent with a Fuller sieve curve in the form $F(d) = (d/d_a)^{n_f}$ where $d_a = 4.75$ mm is the maximum diameter and $n_f = 0.42$ is the Fuller coefficient (Figure 6c). Figure 6a shows an example of particle placement inside the volume of a three-point bending specimen. A lattice system is then defined to describe the interaction between particles by means of a Delaunay tetrahedralization performed with the centers of the spherical particles. In order to define the potential failure locations, a domain tessallation is performed next, which results in a system of polyhedral cells, each of them enclosing a spherical particle. The interaction between cells is described through the triangular facets of the polyhedral cells (Figure 6d) and the generated lattice that links the centers of the particles (also called nodes). Figure 6b shows the position of the LDPM cells in a prism. If $\mathbf{x}_i$ and $\mathbf{x}_j$ are the positions of nodes i and j, adjacent to the facet k, the facet strains are defined as:

$$\mathbf{e}_k = [e_{N_k}\ e_{M_k}\ e_{L_k}]^T = \left[\frac{\mathbf{n}_k^T[\![\mathbf{u}_k]\!]}{l}\ \frac{\mathbf{m}_k^T[\![\mathbf{u}_k]\!]}{l}\ \frac{\mathbf{l}_k^T[\![\mathbf{u}_k]\!]}{l}\right]^T \tag{4}$$

where e_{N_k} is the normal strain component, e_{M_k} and e_{L_k} are the tangential strain components, $[\![\mathbf{u}_k]\!] = \mathbf{u}_j - \mathbf{u}_i$ is the displacement jump at the centroid of the facet k, $l = \|\mathbf{x}_j - \mathbf{x}_i\|_2$ is the distance between the two nodes, $\mathbf{n}_k = (\mathbf{x}_j - \mathbf{x}_i)/l$ and $\mathbf{m}_k$, $\mathbf{l}_k$ are two unit vectors mutually orthogonal in the facet plane projected orthogonally to the node connection. It was demonstrated (Cusatis and Zhou, 2013; Cusatis et al., 2017) that this definition of strains is completely consistent with classical strain definitions in continuum mechanics.

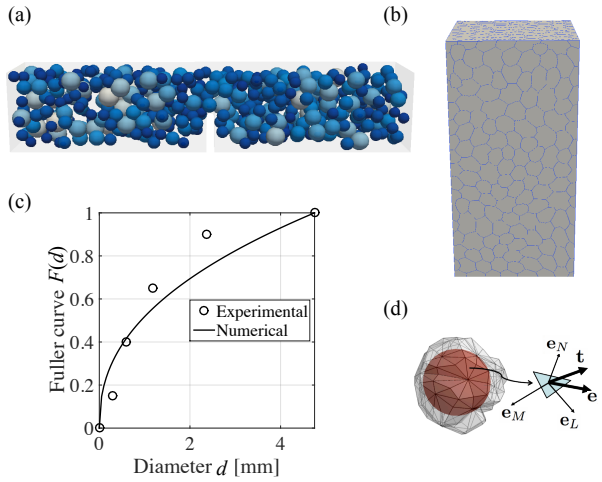

Figure 6. Lattice Discrete Particle Model a) Randomly distributed spherical particles (color gradient indicates the size distribution), b) Position of the LDPM cells in 3D, c) Sieve/Fuller curve, d) LDPM cell and facet strains.

Similarly, one can define the traction vector as:

$$\mathbf{t}_k = [t_{N_k}\ t_{M_k}\ t_{L_k}]^T \tag{5}$$

where t_{N_k} is the normal component, t_{M_k} and t_{L_k} are the shear components. For the sake of readability, the subscript k that designates the facet is dropped in the following equations. In order to describe the behavior of the material, one needs to introduce the constitutive equations imposed at the centroid of each facet. The elastic behavior is defined through linear relations between the normal and shear stresses, and the corresponding strains as $t_N = E_N e_N^*$, $t_M = E_T e_M^*$ and $t_L = E_T e_L^*$, where $e_N^* = e_N - e_N^{eig}$, $e_M^* = e_M - e_M^{eig}$, $e_L^* = e_L - e_L^{eig}$, e_N^{eig}, e_M^{eig}, e_L^{eig} are eigenstrains, $E_N = E_0$ and $E_T = \alpha E_0$. $E_0 = E/(1-2\nu)$ and $\alpha = (1-4\nu)/(1+\nu)$ are the effective normal modulus and the shear-normal coupling parameter respectively where E is Young's modulus and ν is Poisson's ratio.

In order to describe the inelastic behavior, one needs to distinguish three sets of mechanisms.

The first mechanism is the fracturing and cohesive behavior under tension and tension/shear occurring for $e_N^* > 0$. One can define the effective strain as

$$e = \sqrt{e_N^{*2} + \alpha(e_M^{*2} + e_L^{*2})} \tag{6}$$

and the effective stress as

$$t = \sqrt{t_N^2 + \frac{(t_M^2 + t_L^2)}{\alpha}} \tag{7}$$

and write the relationship between the normal and shear stresses, and strains through damage-type constitutive equations as $t_N = t e_N^*/e$, $t_M = \alpha t e_M^*/e$ and $t_L = \alpha t e_L^*/e$.

The effective stress t is defined incrementally as $\dot{t} = E_N \dot{e}$. In addition, a limiting strain-dependent boundary is applied to the effective stress $0 \leqslant t \leqslant \sigma_{bt}(e,\omega)$ in which $\sigma_{bt}(e,\omega) = \sigma_0(\omega)\exp\left[-H_0(\omega)\langle e_{\max} - e_0(\omega)\rangle/\sigma_0(\omega)\right]$ where $\langle x\rangle = \max(x,0)$, ω is the degree of interaction

between shear and normal loading defined through $\tan(\omega) = (e_N^*)/(\sqrt{\alpha}e_T^*) = (t_N\sqrt{\alpha})/(t_T)$. e_T^* is the total shear strain defined as

$$e_T^* = \sqrt{e_M^{*2} + e_L^{*2}} \tag{8}$$

and t_T is the total shear stress defined as

$$t_T = \sqrt{t_M^2 + t_L^2} \tag{9}$$

The maximum effective strain is time dependent and is defined as $e_{\max}^*(\tau) = \sqrt{e_{N,\max}^{*2}(\tau) + \alpha e_{T,\max}^{*2}(\tau)}$ where $e_{N,\max}^*(\tau) = \max_{\tau'<\tau}[e_N^*(\tau')]$ and $e_{T,\max}^*(\tau) = \max_{\tau'<\tau}[e_T^*(\tau')]$. The strength limit of the effective stress that defines the transition between pure tension ($\omega = \pi/2$) and pure shear ($\omega = 0$) is $\sigma_0(\omega) = \sigma_t(-\sin(\omega) + \sqrt{\sin^2(\omega) + 4\alpha\cos^2(\omega)/r_{st}^2})/(2\alpha\cos^2(\omega)/r_{st}^2)$ where $r_{st} = \sigma_s/\sigma_t$ is the shear to tensile strength ratio. The post-peak softening modulus is controlled by a power function called the effective softening modulus $H_0(\omega) = H_t\,(2\omega/\pi)^{n_t}$. Under pure tension, $H_0(\pi/2) = H_t = 2E_0/(l_t/l - 1)$ where H_t is the softening modulus, n_t is the softening exponent. l_t is the tensile characteristic length defined as

$$l_t = \frac{2E_0G_t}{\sigma_t^2} \tag{10}$$

where G_t is the mesoscale fracture energy and σ_t is the tensile strength.

The second set of equations describe the mechanism behind pore collapse and material compaction $e_N^* < 0$. Strain hardening plasticity behavior due to high compressive hydrostatic deformation is described through a strain-dependent boundary $\sigma_{bc}(e_D^*, e_V^*)$ at each facet which limits the normal compressive stress component through the inequality $-\sigma_{bc}(e_D^*, e_V^*) \leqslant t_N \leqslant 0$, where the volumetric strain is defined as

$$e_V^* = \frac{\Delta V}{3V_0} \tag{11}$$

which is computed as the change between the current and the initial volume of each LDPM tetrahedron. While e_V is the same for all the facets of a given tetrahedron, the deviatoric strain defined as

$$e_D^* = e_N^* - e_V^* \tag{12}$$

varies. The strain-dependent boundary is finally defined for three different cases $\sigma_{bc}(e_D^*, e_V^*) = \sigma_{c0}$ for $-e_V^* \leq 0$, $\sigma_{bc}(e_D^*, e_V^*) = \sigma_{c0} + \langle -e_V^* - \varepsilon_{c0}\rangle H_c(r_{DV})$ for $0 \leq -e_V^* \leq e_{c1}$ and $\sigma_{bc}(e_D^*, e_V^*) = \sigma_{c1}(r_{DV})\exp\left[(-e_V^* - e_{c1})H_c(r_{DV})/\sigma_{c1}(r_{DV})\right]$ otherwise, where $r_{DV} = |e_D^*|/e_V^*$ for $e_V^* > 0$ and $r_{DV} = -|e_D^*|/(e_V^* - e_{V0})$ for $e_V^* \leq 0$ in which $e_{V0} = \kappa_{c3}e_{c0}$. $e_{c0} = \sigma_{c0}/E_0$ defines σ_{c0} the material parameter that describes the mesoscale yielding compressive stress, $e_{c1} = \kappa_{c0}e_{c0}$ is the strain at which the rehardening starts, κ_{c0} and κ_{c3} are material parameters and $\sigma_{c1}(r_{DV}) = \sigma_{c0} + (e_{c1} - e_{c0})H_c(r_{DV})$. The function $H_c(r_{DV})$ is written as $H_c(r_{DV}) = H_{c1} + (H_{c0} - H_{c1})/(1 + \kappa_{c2}\langle r_{DV} - k_{c1}\rangle)$ where H_{c0}, H_{c1}, κ_{c1} and κ_{c2} are material parameters.

The third mechanism is the frictional behavior due to compression-shear (again for $e_N^* < 0$). Indeed, the friction provokes an increase in the shear strength. The incremental shear stress in m and l directions are computed as

$$\dot{t}_M = E_T(\dot{e}_M^* - \dot{e}_M^{*p}) \tag{13}$$

and

$$\dot{t}_L = E_T(\dot{e}_L^* - \dot{e}_L^{*p}) \tag{14}$$

where $\dot{e}_M^{*p} = \dot{\lambda}\partial\varphi/\partial t_M$, $\dot{e}_L^{*p} = \dot{\lambda}\partial\varphi/\partial t_L$, and φ the plastic potential is defined as $\varphi = \sqrt{t_M^2 + t_L^2} - \sigma_{bs}(t_N)$. The shear strength σ_{bs} is a nonlinear frictional law written as $\sigma_{bs}(t_N) = \sigma_s + (\mu_0 - \mu_\infty)\sigma_{N0}[1 - \exp(t_N/\sigma_{N0})] - \mu_\infty t_N$ where μ_0 and μ_∞ are the initial and final internal friction coefficients and σ_{N0} is the normal stress which corresponds to the transition from μ_0 to μ_∞.

Last but not least, the governing equations are completed by writing the equilibrium of each LDPM cell:

$$\sum_{k\in\mathcal{F}_I} A_k\mathbf{t}_k + V_I\mathbf{b} = \mathbf{0}, \quad \sum_{k\in\mathcal{F}_I} A_k\mathbf{c}_k \times \mathbf{t}_k = \mathbf{0} \tag{15}$$

where $\mathcal{F}_I$ is the set containing all the facets of a generic polyhedral cell I, A_k is the area of the facet k, $\mathbf{c}_k$ is the vector representing the distance between the center of the facet k and the center of the cell, V_I is the cell volume and $\mathbf{b}$ is the external body forces applied to the cell.

In the original LDPM publications, the mesoscale parameters E_0, σ_t, r_{st}, l_t, σ_{c0}, σ_{N0}, α, H_{c0}/E_0, H_{c1}/E_0, κ_{c0}, κ_{c1}, κ_{c2}, κ_{c3}, μ_0 and μ_∞ are constant. In this study, however, the interest is the evolution of the mechanical behavior at early age. To account for early age effects, LDPM was recently equipped with an aging model (Wan et al., 2016).

One can write

$$E_0 = E_0^\infty\lambda \tag{16}$$

$$\sigma_t = \sigma_t^\infty\lambda^{n_a},\ \sigma_{c0} = \sigma_{c0}^\infty\lambda^{n_a},\ \sigma_{N0} = \sigma_{N0}^\infty\lambda^{n_a} \tag{17}$$

$$r_{st} = r_{st}^\infty\lambda^{m_a} \tag{18}$$

$$l_t = l_t^\infty(k_a(1-\lambda)+1) \tag{19}$$

where λ is the aging degree (fully described in the next paragraph), E_0^∞, σ_t^∞, σ_{c0}^∞, σ_{N0}^∞, r_{st}^∞ and l_t^∞ are the asymptotic values of the aforementioned parameters, n_a, m_a and k_a are material parameters. The other parameters are assumed to be age-independent. It is worth mentioning that in the work of Wan et al. (2016), r_{st} was taken as age-independent, i.e. assuming $m_a = 0$.

Cement hydration of mortar that causes the evolution in strength is described through the Hygro-Thermo-Chemical (HTC) model. The model computes at any age the heat transfer and moisture diffusion in concrete and mortar, through coupled diffusion equations involving the variation of temperature T, moisture h, moisture permeability D_h, cement hydration degree α_c, evaporable water w_e and other material properties. The relevant sets of equations, namely Fick's law, moisture permeability equation, unit volume mass balance, sorption/desorption isotherm, Fourier's law and enthalpy balance equation are reported in the Appendix.

The chemical reactions involving the four different cement clinker phases and water are accounted for in average by computing the so-called degree of hydration α_c through the following empirical differential equation (Di Luzio and Cusatis, 2009a):

$$\dot{\alpha}_c = A_{c1}\left(\frac{A_{c2}}{\alpha_c^\infty} + \alpha_c\right)(\alpha_c^\infty - \alpha_c)e^{-\frac{\eta_c\alpha_c}{\alpha_c^\infty}}\beta(h)e^{-\frac{E_{ac}}{RT}} \tag{20}$$

where A_{c1}, A_{c2} and η_c are material parameters, α_c^∞ is the asymptotic hydration degree that can be approximately calculated as $\alpha_c^\infty = 1.031(w/c)/(0.194 + (w/c))$ and $\beta(h) = [1 + (5.5 - 5.5h)^4]^{-1}$ is an empirical function that describes the effect of moisture content, E_{ac} is the hydration activation energy.

Once the degree of hydration is computed, one needs to relate it to the mechanical properties of mortar. It is well accepted that the strength evolution depends on the degree at which the chemical reactions occurred but also the curing temperature. One can thus introduce an internal variable λ, the aging degree, that takes into account both effects through the following equation (Di Luzio and Cusatis, 2013):

$$\dot{\lambda} = \dot{\alpha_c}\Big[A_{\lambda 0} + A_\lambda(\alpha_c^\infty + \alpha_0 - 2\alpha_c)\Big]\left(\frac{T_{max} - T}{T_{max} - T_{ref}}\right)^{n_\lambda} \tag{21}$$

for $\alpha > \alpha_0$ and $\dot{\lambda} = 0$ for $\alpha \leqslant \alpha_0$, where α_0 is the value of the hydration degree at which mortar starts to get a solid consistency, $A_{\lambda 0} = (\alpha_c^\infty - \alpha_0)^{-1}$, A_λ is a material parameter, T_{max} and T_{ref} are the maximum temperature at which mortar can harden and the room temperature respectively.

In terms of numerical implementation, the hygro-thermo-chemo-mechanical coupling is performed as follows: once the geometry of the specimen is considered, a tetrahedral finite element (FE) mesh is generated. The HTC model equations are solved numerically and the state variables such as temperature, moisture content, degree of hydration and aging degree are computed at the nodes. Then, their values are interpolated to the nearest facet centroids by using the FE shape function associated to each tetrahedron. Each facet now has at any time step the updated value of the aging degree, which allows to update the mesoscale LDPM parameters through the aging equations.

The ASR model describes the gel formation and expansion at the aggregate level. The model distinguishes for each aggregate particle the gel formation and the effect of water imbibition. It is important to point out that smaller length scale processes are averaged and only phenomenologically represented; this includes 1) the actual chemistry of gel formation, 2) the micro-transport phenomena of ions in gel, pores and cracks, 3) the gel transport in pores and cracks. Since the silica present in the aggregate needs to be in contact with the surrounding water and alkali ions present in the cement paste for the ASR gel to be formed, it can be assumed that gel formation is governed by a diffusion process. This approach is based on the observation that the time scale of the alkali-silica reaction is much shorter than the one of diffusion. For very small particles, this assumption might not be accurate (Multon and Sellier, 2016). However, for computational cost considerations, the model proposed in this study only focuses on the coarser portion of the particle size distribution for which, indeed, the diffusion process is dominant. The effect of the particles not directly resolved is included indirectly in the parameters of the model constitutive equations. The process can be described by the following radial diffusion equation for each spherical particle of diameter D (Bažant and Steffens, 2000):

$$\dot{z} = -\frac{w_e}{z - \frac{2z^2}{D}}\kappa_{z0} e^{\frac{E_{ag}}{RT_0} - \frac{E_{ag}}{RT}} \tag{22}$$

where z is the diffusion front position, w_e is the evaporable water defined in the Appendix (see Equations 27 and 28), k_{z0} is a material parameter, and E_{ag} is the gel diffusion activation energy.

The mass of gel M_g formed surrounding one aggregate is then computed as (Alnaggar et al., 2017):

$$M_g = \frac{\kappa_a \rho_g \pi}{6}(D^3 - 8z^3) \tag{23}$$

where ρ_g is the density of the ASR gel, $\kappa_a = \min(\langle c_a - c_{a0}\rangle/(c_{a1} - c_{a0}), 1)$ where c_a is the macroscopic alkali concentration and c_{a1} is the saturation alkali content for which the reaction is complete. c_{a0} is the threshold alkali content at which no expansion is observed. Although it was found (Kim and Olek, 2014; Kim et al., 2015) that this threshold depends on several factors, including but not limited to calcium concentration, the present study assumes, as a simplification, c_{a0} to be constant.

Once the gel is created, it is assumed to imbibe water. For a fixed temperature, the water imbibition rate $\dot{M}_i$ is characterized as a linear function of the gel mass M_g as follows (Alnaggar et al., 2017):

$$\dot{M}_i = \frac{C_i}{\delta^2}[M_g \kappa_{i0} e^{\frac{E_{ai}}{RT_0} - \frac{E_{ai}}{RT}} - M_i] \tag{24}$$

The bulk diffusivity of imbibed water C_i includes the contribution of the cement paste, as well as the external rim of the aggregate particle: $C_i = C_{i0}\exp(E_{aw}/(RT_0) - E_{aw}/(RT))$. E_{ai} and E_{aw} are the activation energies of respectively the imbibition capacity and the diffusion process. κ_{i0} and C_{i0} are material parameters. δ characterizes the thickness through which water is transported from the cement paste to the surrounding of the aggregate where the ASR gel lies. Petrographic observations (Figure 3b) suggests that such a distance is in the order of a few micrometers (which is confirmed later by calibration results). It is reasonable to assume that the water present in a generic location has approximately the same distance to travel to reach each of the surrounding aggregate particles of the same size. One can thus assume that $\delta = \alpha_M D$ where α_M is a proportionality parameter as introduced by Alnaggar et al. (2017). One can then define $\tilde{C}_i = C_i/\alpha_M^2$ in Equation 24.

To accommodate the change in volume due to water imbibition, material expansion must occur. In the simple case of two interacting particles, the expansion can be simulated by a change in radius of both particles, which, in turn, generates a so-called imposed strain or LDPM eigenstrain $\mathbf{e}_k^a$ at the adjacent facet k. By assuming negligible the LDPM shear eigenstrains $e_{M_k}^a$ and $e_{L_k}^a$, only the contribution of the normal eigenstrain $e_{N_k}^a$ is taken in account. By considering δ_c the equivalent thickness of capillary pores surrounding the aggregate and accessible to the gel (assumed constant and independent of D, one can define the amount of imbibed water as $\langle M_i - M_i^0\rangle$ where $M_i^0 = (4\pi\rho_w/3)((r+\delta_c)^3 - r^3)$. One can then write the increase in radius $r_i = [3\langle M_i - M_i^0\rangle/4\pi\rho_w + r^3]^{1/3}$. Then, by computing the rate of increase $\dot{r}_i = [\dot{M}_i/(4\pi\rho_w)][3\langle M_i - M_i^0\rangle/4\pi\rho_w + r^3]^{-2/3}$. Finally, the imposed normal strain due to ASR can be defined as

$$\dot{e}_{N_k}^a = \frac{\dot{r}_{i1} + \dot{r}_{i2}}{l} \tag{25}$$

where r_{i1} and r_{i2} are the increases in radii of the aggregate particles 1 and 2 at a distance l from each other. By adding the effect of thermal deformations, the total normal eigenstrain can be written as $\dot{e}_{N_k}^{eig} = \alpha_T \dot{T} + \dot{e}_{N_k}^a$.

Calibration process

The response of the overall computational framework depends on three sets of parameters that needs to be identified by means of experimental data or assumed on the basis of existing literature. The work flow of the identification process is described in this section.

Keeping in mind that the final objective is to be able to predict the deterioration of mortar affected by ASR (mechanical properties of samples 80A) while taking in account the aging effect, data relevant to samples 23A, 23W and samples 80W, as well as the expansion measurement of samples 80A were used

for model calibration. The hydration model was calibrated from calorimetric tests. The aging model was calibrated from the compression and fracture behavior of samples 23W and 80W at age 6 days and 16 days (since samples 23A and samples 23W exhibit the same behavior, the choice was made to focus only on samples 23W). Finally, the ASR model was calibrated from the expansion measurements of samples 80A. The mechanical properties obtained for samples 80A were then used for the validation process in which blind predictions are carried out without adjusting the model parameters.

In order to calibrate the hydration component of the HTC model, the actual setup of the calorimetric tests was replicated (Figure 7b) by using a tetrahedral mesh with a mesh refinement comparable to the associate LDPM discretization for the center of the calorimeter where the mortar specimen is located. The boundary conditions consisted of applying room temperature (23°C) on the external surfaces of the mesh. The insulation of the calorimeter was expanded rigid rubber and its thermal characteristics were estimated, i.e. values of the heat capacity and density were taken from the literature: $c_T^{cal} = 1680$ J kg^{-1} K^{-1} and $\rho^{cal} = 72$ kg m^{-3}, respectively. The density of mortar was measured to be $\rho = 2591$ kg m^{-3}. The heat conductivity of the calorimeter λ_T^{cal} and the cement hydration parameters A_{c1}, A_{c2} and η_c were identified simultaneously by fitting the experimental data and yielding the following values $\lambda_T^{cal} = 6.6 \times 10^{-2}$ W m^{-1} K^{-1}, $A_{c1} = 6 \times 10^{7}$ h^{-1}, $A_{c2} = 7 \times 10^{-3}$, $\eta_c = 6.5$. The following parameters were estimated from Di Luzio and Cusatis (2009b): $E_{ac} = 45646$ J mole^{-1}, $D_0 = 1.9 \times 10^{-6}$ kg m^{-1} h^{-1}, $D_1 = 2.5 \times 10^{-3}$ kg m^{-1} h^{-1}, $n = 3.25$, $E_{ad} = 22449$ J mole^{-1}, $k_{vg}^c = 0.2$ and $g_1 = 1.5$. Figure 7c shows the experimental data (average of three samples), as well as the calibrated response of the HTC model. Figure 7d,e,f show the temperature distribution after 4, 11 and 21 hours from casting. One can clearly see the temperature increase and the subsequent decrease as the heat transfer occurs through the insulation. The aging model describing the mechanical behavior

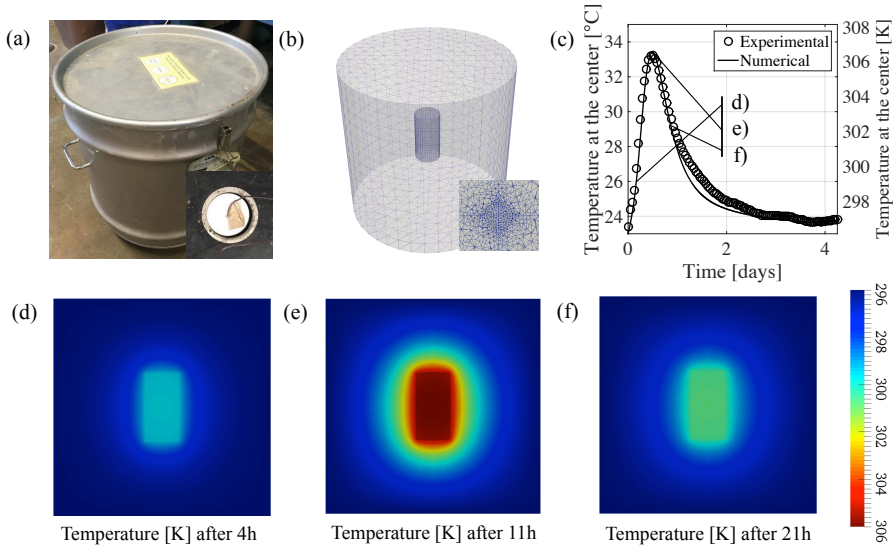

Figure 7. Semi-adiabatic calorimetric test a) Actual setup, b) Replication for calibration, c) Calibration results, d) Temperature after 4 hours, e) Temperature after 11 hours, f) Temperature after 21 hours.

of mortar due to cement hydration can now be calibrated. In addition to the applied load, data from the uniaxial unconfined compression tests include measurements of machine stroke stroke, which, however,

cannot be used modulus identification since it includes the effect of loading apparatus deformability. An alternative, adopted in this study, consists of calibrating the elastic properties from the load-CMOD curve of the three-point bending tests. Since the CMOD extensometer is directly attached to the specimen, any recorded displacement is associated to strains in the specimen and is independent on the deformability of the load apparatus. E_0 is calibrated for samples 23W and samples 80W at 6 days and 16 days from the elastic portion of the load-CMOD curve of the three-point bending tests. One needs then to get the aging degree as an output of the HTC model in order to identify E_0^{∞} in Equation 16. Since the samples are small, the degree of hydration and temperature are spatially uniform which in turn leads λ to be uniform throughout the specimen (see Figure 8). An average of the aging degree values at different locations thus gives an accurate estimation for the whole specimen. The choice was made to select a small cube at the center of the prism and take the average of the aging degree values at the selected nodes. A_λ is first calibrated for the samples at room temperature, where the exponent n_λ vanishes. Then n_λ is calibrated on the samples at 80°C. Assuming the value of $\alpha_0 = 0.15$ and $T_{max} = 100$°C from existing literature (Di Luzio and Cusatis, 2013) and $T_{ref} = 23$°C, one can identify the aforementioned parameters: $A_\lambda = 0.5$, $n_\lambda = 0.65$ and $E_0^{\infty} = 66500$ MPa. Figure 8c,d,e,f show the aging degree values distribution on the compression samples, for samples 23W and 80W at 6 and 16 days respectively. Figure 8a shows the normal modulus as a function of the aging degree. By plotting E_0 as a function of the degree of hydration (Figure 8b), one can notice that the experimental data nicely fit to the two curves, corresponding to the two temperatures. The full calibration of samples 23W and samples 80W at 6 and

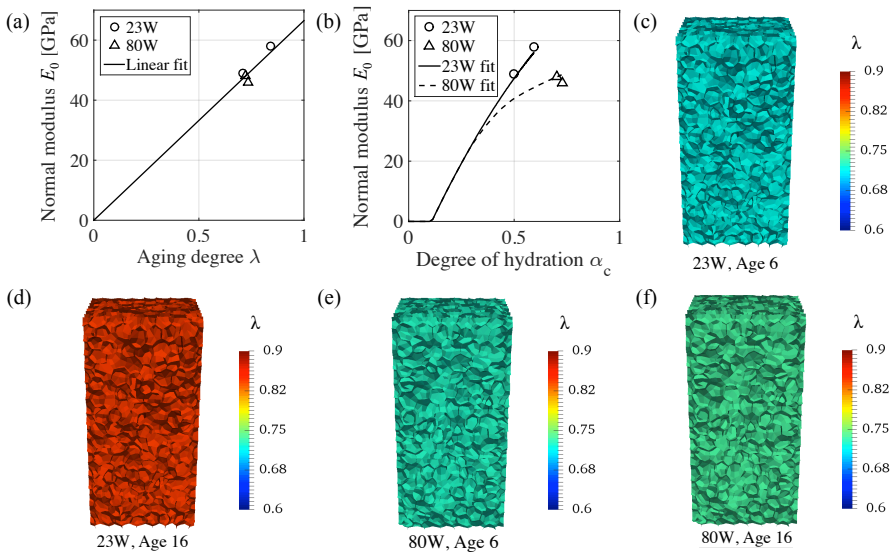

Figure 8. Aging model calibration a) Normal modulus function of the aging degree, b) Normal modulus function of the degree of hydration, c) Aging degree for samples 23W at age 6 days, d) Aging degree for samples 23W at age 16 days, e) Aging degree for samples 80W at age 6 days, f) Aging degree for samples 80W at age 16 days.

16 days, in compression and three point bending setups for three different experimental samples and three LDPM meshes is then performed. The identified values for the aging model are: $\sigma_t^{\infty} = 9.53$ MPa, $r_{st}^{\infty} = 1.94$, $l_t^{\infty} = 31.92$ mm, $n_a = 1.166$, $m_a = 1.5$, $k_a = 3.577$. In general, in order to calibrate

fully the LDPM mesoscale parameters, it is necessary to capture the behavior of the concrete/mortar material in tension, compression but also under confinement. Due to the lack of experiments for the later behavior, the following LDPM parameters are assumed based on existing literature (Cusatis et al., 2011b; Alnaggar et al., 2013): $\alpha = 0.25$, $H_{c0}/E_0 = 0.4$, $H_{c1}/E_0 = 0.1$, $\kappa_{c0} = 2$, $\kappa_{c1} = 1$, $\kappa_{c2} = 5$, $\kappa_{c3} = 0.1$, $\mu_0 = 0.2$, $\mu_\infty = 0$. Moreover, $\sigma_{c0}^{\infty} = 183$ MPa and $\sigma_{N0}^{\infty} = 734$ MPa are computed by assuming that for samples 23W at age 6 days, $\sigma_{c0} = 123$ MPa and $\sigma_{N0} = 500$ MPa. Figure 9 shows the calibrated response curves. The gray area represents the upper and lower bounds of the experimental curves and the error bars show the scatter in the numerical response, due to the randomness of the particle placement in LDPM.

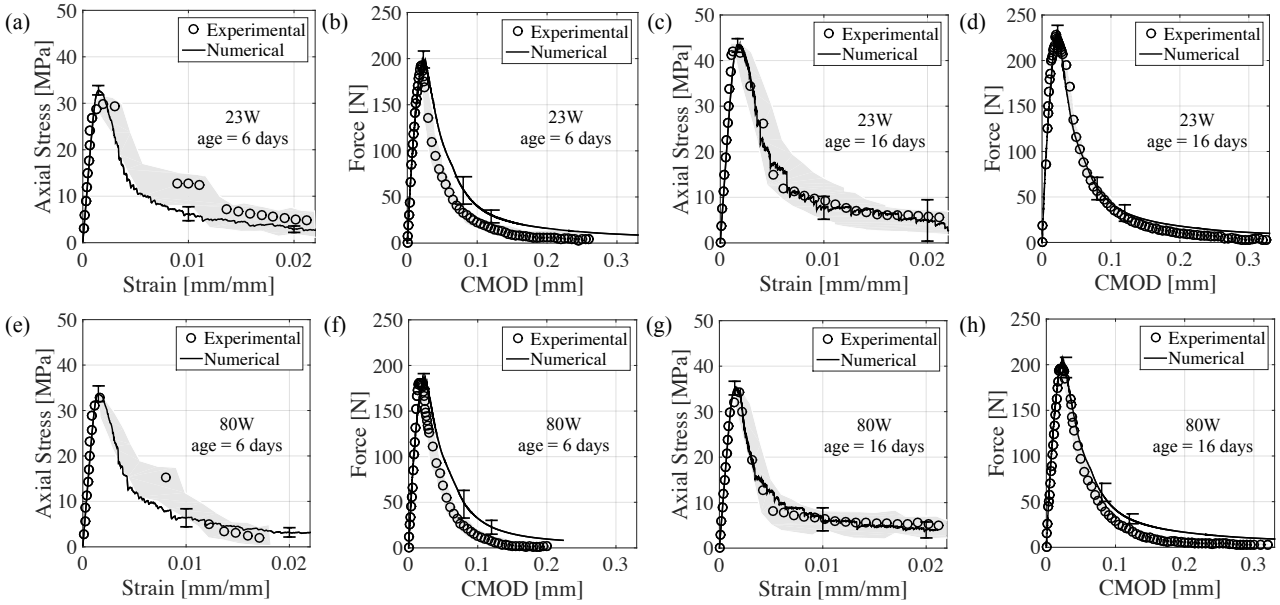

Figure 9. LDPM Calibration of samples 23W and samples 80W. a) and b) Compression and Three point bending tests on samples 23W at age 6 days, c) and d) Compression and Three point bending tests on samples 23W at age 16 days, e) and f) Compression and Three point bending tests on samples 80W at age 6 days, g) and h) Compression and Three point bending tests on samples 80W at age 16 days.

Last but not least, the ASR model is calibrated. It is worth mentioning that this calibration is done while the coupling HTC-LDPM is executed. Indeed, in order to fit the expansion curve of samples 80A, one needs to consider aging that is accompanying ASR expansion and damage. Samples 80A were kept under saturated conditions, thus the following expression can be used for the evaporable water: $w_e = w_0 - 0.188\alpha_c c$ (Di Luzio and Cusatis, 2009a). Moreover, the alkali content is much higher than what is needed to complete the reaction with the present silica, thus $k_a = 1$. Since the temperature is constant, $T = T_0 = 80°\text{C}$, all the Arrhenius functions in Equations 22, 24 and in the expression of C_i are equals to unity. The density of the ASR gel was estimated to be $\rho_g = 252.77$ kg m^{-3} based on the silica content $c_s = 161.4$ kg m^{-3} (Alnaggar et al., 2013). By taking into account the effects of gel formation and water imbibition on expansion, the following parameters were identified: $k_z = 8.04$ cm^5 kg^{-1} day^{-1} and $k_i = 0.12$ that control the expansion curve amplitude, $\tilde{C}_i = 0.69$ mm^2 day^{-1} and $\delta_c = 0.0052$ mm that affect the initial part and slope of the curve. Figure 10 shows the curve fitting of the expansion measurements of samples 80A, performed with the average of three different LDPM meshes.

Tables 5, 6 and 7 in the Appendix report the identified or estimated parameters involved in the modeling of the hygro-thermo-chemical process, the aging and mechanical behavior and the alkali silica reaction.

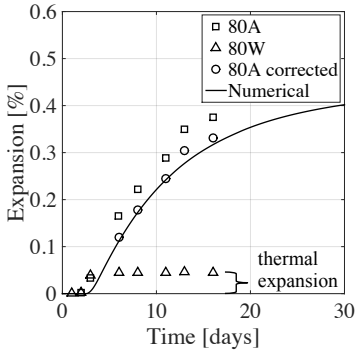

Figure 10. ASR model calibration on expansion measurements

PREDICTION RESULTS AND DISCUSSION

Once all the parameters are either calibrated or estimated based on existing literature, samples 80A were simulated in compression and three point bending at age 6 days and 16 days, as pure prediction. Figure 11a,e and Figure 12a,b show the results for compression at age 6 days and 16 days and three point bending at age 6 days and 16 days of samples 80A. The error bars represent the scatter in the numerical response. One can observe a very good agreement with the experimental data. At age 6 days, the coupled models were able to capture perfectly the elastic slope, the peak values and also the post-peaks. At age 16 days, it appears that the model predicts a slightly higher damage degree, mostly in terms of elastic modulus reduction. Figure 11b,c and d show the evolution of the mesoscale crack opening, after 72, 108 and 144 hours after casting. One can notice that the cracks are uniformly distributed in agreement with the experimental evidences. The values of the cracks go from 1 micrometer, up to about 100 micrometers for the specimen at age 16 days. The values of the normal ASR eigenstrain vary from around 0 to about 0.006. It is interesting to compare the mesoscale crack opening in Figure 11d,f and the imposed normal strain in Figure 12c at the same mortar age. Indeed, as the imposed normal strain at the facets increases in time throughout the expansion period, the crack opening increases simultaneously. Moreover, the LPDM mesoscale parameters also evolve in time, at the same facets. This leads to a complex process where the crack opening is the result of both the imposed normal strain and the changing constitutive equations at each time step due to the evolution in the LDPM mesoscale parameters. Figure 11 shows the prediction in compression for samples 80A at age 16 days (Figure 11e), the mesoscale crack opening distribution throughout the specimen at age 16 days (Figure 11f), the change in crack distribution when the load is being applied (Figure 11g), and finally the prism failure under vertical loading (Figure 11h). One can notice that the ASR damage was such that a horizontal crack was formed at age 16 days. This is the same mechanism that leads full mortar bars to expand. When the load starts to be applied, the crack that was formed earlier gets closed. The stress strain curve describes this phenomena (Figure 11e) as it features an initial slope of angle γ_1 and a second slope of angle γ_2, where $\gamma_1 < \gamma_2$. In the experimental testing, the same phenomenon is expected to happen, however it is impossible to distinguish the effect of the

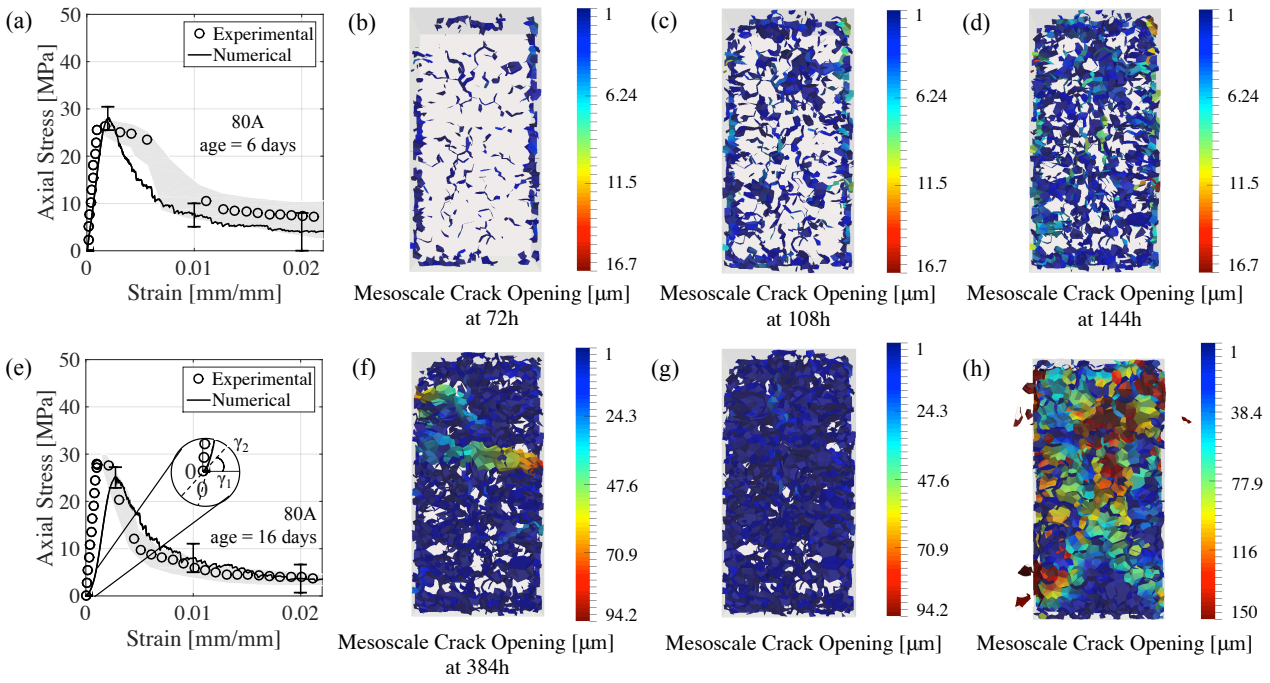

Figure 11. Prisms behavior under ASR a) Compression test prediction of samples 80A at age 6 days, b) Total crack opening after 72h, c) Total crack opening after 108h, d) Total crack opening after 144h, e) Compression test prediction of samples 80A at age 16 days, f) Crack open at age 16 days, g) Closed crack due to applied vertical load, h) Prism failure under uniaxial unconfined compression test.

machine settlement while loading and a crack closing due to ASR, since the former effect is dominant. In all experimental stress-strain curves, the initial non-linearity was removed following standard processing of compression test data. Figure 11h shows a typical failure on a 1:2 ratio prism specimens, when high friction is used between the top surface of the prism and the loading platen in order to fully replicate the same boundary conditions of the experiments.

When dealing with ASR damage, it is crucial to consider the right boundary conditions, the right geometries etc. Indeed, the normal eigenstrains induce a considerable anisotropy in the mesoscale structure. Figure 12d is a good example of such a behavior as the figure shows at the same age (16 days) the crack propagation when the load is applied for a squared-notched beam (left figure) and a rounded-notched beam (right figure) more representative of reality. Since ASR occurs during these 16 days, cracks localize at the sharp edge of the squared notch and propagate along the pre-existing crack pattern when testing the beams (Figure 12d,left). For the rounded notch (Figure 12d,right), the crack during loading is less affected by prior localized crack evolution. However, one can notice in Figure 12b that the softening behavior is different from Figure 12a. The softening branch is more ductile because the crack does not propagate perfectly vertically, even though a rounded notch is considered. Additional improvement in the response could be obtained by increasing the resolution of the model (minimum aggregate size in LDPM), which, however, would lead to an increase of the computational cost.

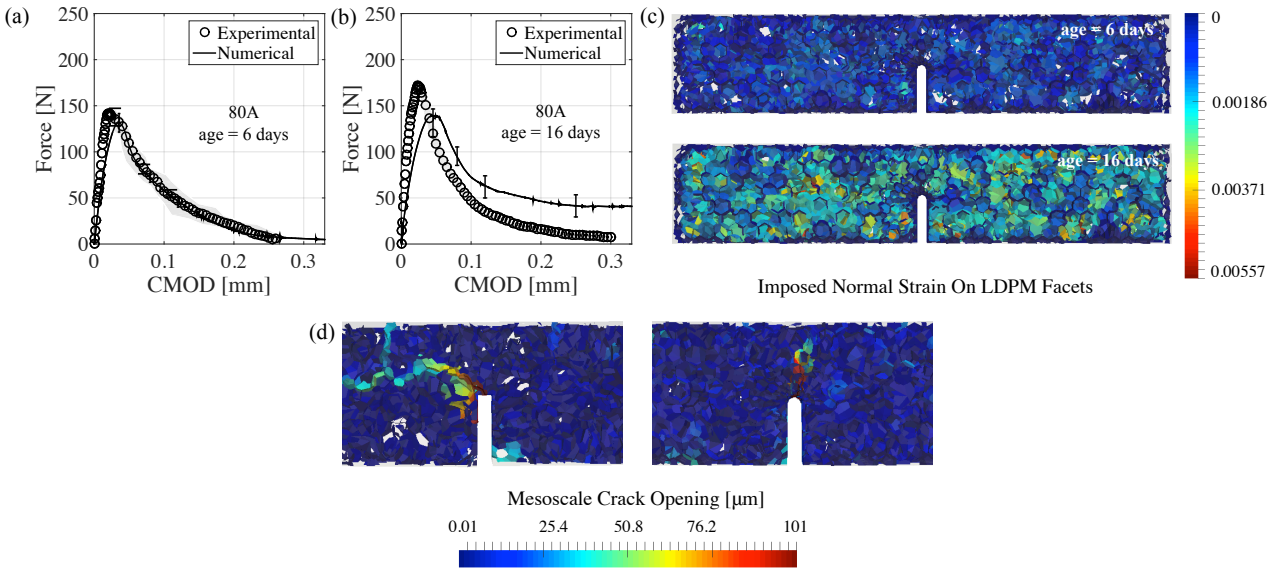

Figure 12. Notched beams behavior under ASR a) Three point bending test prediction of samples 80A at age 6 days, b) Three point bending test prediction of samples 80A at age 16 days, c) Imposed normal strains distributed throughout the beam at 6 days (upper figure) and 16 days (lower figure), d) Influence of the notch geometry.

In order to understand strengthening and deterioration processes occurring in the studied mortars, all the results from expansion measurements, petrographic analyses and mechanical testings have to be considered together. One can identify multiple factors affecting the behavior of mortar: alkali content, temperature, age of mortar, micro-cracking and presence of alkali silica gel. It is important to note that commonly relevant factors are here unchanged for all performed experiments and simulations. For instance, among other parameters, this study did not address the effect of aggregate type (silica content, shape or stiffness) or cement type on ASR.

The complexity of the analysis comes from the fact that the listed factors are related to each other and identifying their interaction provides a better understanding of the effect of ASR.

Figure 13 shows in a synthetic way the comparison of the mechanical properties of mortar at age 6 and 16 days after casting, for the four environmental conditions. It was shown from length change measurements and petrography that there is no alkali silica reaction in samples 23W, 23A and 80W. Since the behavior of samples 23W and 23A is very similar, they will be referred thereinafter as samples 23, which constitute the reference case at room temperature. The reference case at 80°C is sample 80W, for which no ASR gel was found. However, samples 80W show thermal expansion and a different evolution of mechanical properties. Samples 80A are the only ASR-affected samples: they exhibit high expansion and the presence of ASR gel was confirmed. The high expansion is mostly due to ASR development with a little contribution from the thermal expansion.

By comparing samples 23 at age 6 and 16 days, one can highlight the effect of cement hydration and what is commonly called aging. Table 3 shows an increase of 36.6%, 46.4%, 12.8% and 56.8% for compressive strength, fracture energy, nominal fracture stress and tensile strength, respectively.

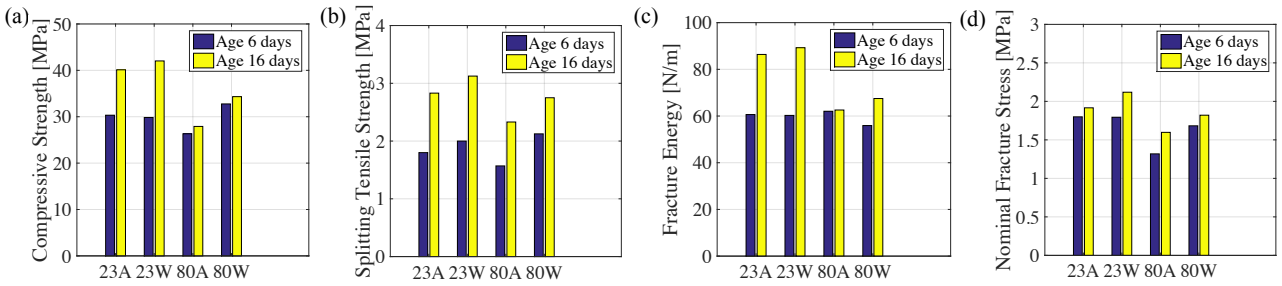

Figure 13. Variation in time of mechanical properties for the four different environmental conditions a) Compressive strength, b) Splitting tensile strength, c) Fracture strength, d) Nominal fracture stress.

The aging process is however altered, i.e. accelerated by the effect of temperature. At age 6 days, one can compare the mechanical behavior of samples 23 and samples 80W: the compressive and tensile strength are higher for samples 80W, while the fracture energy and the nominal fracture stress are similar. However, at age 16, the compressive strength and fracture properties are higher in samples 23 than in samples 80W. Indeed, the higher temperature acts like a catalyst on the hydration process, such that mortar acquires strength faster. At later ages, the strength gained by additional heat is lower than the one acquired by a mortar cured at room temperature. This is mostly due to a different type of C-S-H (higher apparent density due to a decrease in bound water) created at higher temperatures (Gallucci et al., 2013). This effect is well reproduced by using the aging degree concept. The increase of compressive strength, fracture energy, nominal fracture stress and tensile strength for samples 80W from age 6 days to 16 days are 4.8%, 20%, 8.3% and 29.7% (Table 4), respectively, which are lower values than for samples 23.

In order to understand the effect of ASR, one needs to decouple it with the evolution of the micro-structure due to hydration at high temperature. Free expansion measurements of samples 80A, as well as the associated mechanical properties are compared to the reference companion samples 80W. Indeed, samples 80W were found to be ASR-free by use of petrographic analysis, but are subjected to the same micro-structural changes associated with the hydration kinetics and reaction products as 80A samples. Thus, the relative difference between samples 80W and 80A is in the presence of ASR gel, i.e., the damage due solely to ASR. For instance, as expansion occurs, the fracture energy G_F remains somehow constant for samples 80A. However, this evolution needs to be compared to its associated reference case, sample 80W, which does see an increase of G_F: one can then conclude that the constant fracture energy result in the reactive case is misleading if viewed separately from the non-reactive case behavior. All these coupled effects are well captured by the presented computational framework.

Conclusion

An experimental program was conducted on mortar, following the ASTM C1260, in order to study the effect of Alkali Silica Reaction and its effect on the evolution of mechanical properties. Mortar strengthening due to cement hydration appears to play a large role and its effect was also investigated. A computational program followed, introducing a complete coupled model, which includes the mechanical

behavior (Lattice Discrete Particle Model), mortar strengthening due to cement hydration (Hygro-Thermo-Chemical model), its evolution in time (aging model) and the expansion due to ASR (ASR model). Both experimental and numerical results show that:

- Aging occurs for samples 23W, 23A and 80W but ASR affects only samples 80A. The mechanical properties of samples 80A are lower than the three other cases at the same age. This difference is a direct consequence of ASR-induced damage.

- An increase of all the mechanical properties from age 6 days to age 16 days was observed for all the four cases. Indeed, although alkali silica reaction occurs and its kinetics accelerates in time as found by petrography and expansion measurements, the hydration process counter-balances ASR deterioration.

Finally, the comparison between experiments and computations clearly demonstrate the excellent modeling and predictive capabilities of the adopted multiphysics computational framework.

Acknowledgements

The authors gratefully acknowledge the Ministry of Transportation Ontario for providing Spratt aggregates, Victoria Jennings, Senior Petrographer at CTLGroup (Skokie, IL, USA) for her great guidance in performing the petrographic analyses and Kaijing Luo, visiting PhD student from China University of Mining and Technology (Beijing, China) for the help provided in performing the experiments.

Funding

This effort was sponsored by the Nuclear Regulatory Commission (NRC), Award Number NRC-HQ-60-14-FOA-0001.

Declaration of conflicting interests

The Authors declare that there is no conflict of interest.

References

Alnaggar, M., Cusatis, G., and Di Luzio, G. (2013). "Lattice discrete particle modeling (ldpm) of alkali silica reaction (asr) deterioration of concrete structures." *Cement and Concrete Composites*, 41, 45–59.

Alnaggar, M., Liu, M., Qu, J., and Cusatis, G. (2015). "Lattice discrete particle modeling of acoustic nonlinearity change in accelerated alkali silica reaction (asr) tests." *Materials and Structures*, 1–23.

Alnaggar, M., Di Luzio, G., and Cusatis, G. (2017). "Modeling time-dependent behavior of concrete affected by alkali silica reaction in variable environmental conditions." *Materials*, 10(5), 471.

ASTM-C1260-07, Standard test method for potential alkali reactivity of aggregates (mortar-bar method), ASTM International West Conshohocken, PA, 2014, www.astm.org (2007).

Bangert, F., Kuhl, D., and Meschke, G. (2004). "Chemo-hygro-mechanical modelling and numerical simulation of concrete deterioration caused by alkali-silica reaction." *International Journal for Numerical and Analytical Methods in Geomechanics*, 28(7-8), 689–714.

Bažant, Z. P. and Planas, J. (1997). *Fracture and size effect in concrete and other quasibrittle materials*, Vol. 16. CRC press.

Bazant, Z. P. and Steffens, A. (2000). "Mathematical model for kinetics of alkali–silica reaction in concrete." *Cement and Concrete Research*, 30(3), 419–428.

Bažant, Z. P. and Rahimi-Aghdam, S. (2016). "Diffusion-controlled and creep-mitigated asr damage via microplane model. i: Mass concrete." *Journal of Engineering Mechanics*, 143(2), 04016108.

Ben Haha, M., Mechanical Effects of Alkali-Silica Reaction in Concrete Studied by SEM-Image Analysis, Ph.D. thesis, Thesis, 2006.

Bernard, O., Ulm, F.-J., and Lemarchand, E. (2003). "A multiscale micromechanics-hydration model for the early-age elastic properties of cement-based materials." *Cement and Concrete Research*, 33(9), 1293–1309.

Bullard, J. W., Jennings, H. M., Livingston, R. A., Nonat, A., Scherer, G. W., Schweitzer, J. S., Scrivener, K. L., and Thomas, J. J. (2011). "Mechanisms of cement hydration." *Cement and Concrete Research*, 41(12), 1208–1223.

Capra, B. and Sellier, A. (2003). "Orthotropic modelling of alkali-aggregate reaction in concrete structures: numerical simulations." *Mechanics of materials*, 35(8), 817–830.

Cebeci, O., S. Al-Noury, W. Mirza, Strength and drying shrinkage of masonary mortars in various temperature-humidity environments, Cement and Concrete Research 19 (1989) 53–62.

Ceccato, C., Salviato, M., Pellegrino, C., and Cusatis, G. (2017). "Simulation of concrete failure and fiber reinforced polymer fracture in confined columns with different cross sectional shape." *International Journal of Solids and Structures*, 108, 216–229.

Cervera, M., Oliver, J., and Prato, T. (1999). "Thermo-chemo-mechanical model for concrete. i: Hydration and aging." *Journal of engineering mechanics*, 125(9), 1018–1027.

Cervera, M., Oliver, J., and Prato, T. (2000). "Simulation of construction of rcc dams. i: temperature and aging." *Journal of Structural Engineering*, 126(9), 1053–1061.

Chatterji, S., A. D. Jensen, N. Thaulow, P. Christensen, Studies of alkali-silica reaction. part 3. mechanisms by which nacl and ca (oh) 2 affect the reaction, Cement and concrete research 16 (1986) 246–254.

Chatterji, S., N. Thaulow, A. Jensen, Studies of alkali-silica reaction. part 4. effect of different alkali salt solutions on expansion, Cement and Concrete research 17 (1987) 777–783.

Charlwood, R., A review of alkali aggregate in hydro-electric plants and dams., Hydropower Dams 5 (1994) 31–62.

Clark, L., Structural aspects of alkali-silica reaction, Structural Engineering Review 2 (1990) 81–87.

Comby-Peyrot, I., Bernard, F., Bouchard, P.-O., Bay, F., and Garcia-Diaz, E. (2009). "Development and validation of a 3d computational tool to describe concrete behaviour at mesoscale. application to the alkali-silica reaction." *Computational Materials Science*, 46(4), 1163–1177.

Comi, C., Fedele, R., and Perego, U. (2009). "A chemo-thermo-damage model for the analysis of concrete dams affected by alkali-silica reaction." *Mechanics of Materials*, 41(3), 210–230.

Cruz, C.R., M. Gillen, Thermal expansion of portland cement paste, mortar and concrete at high temperatures, Fire and materials 4 (1980) 66–70.

Cusatis, G., Pelessone, D., and Mencarelli, A. (2011). "Lattice discrete particle model (ldpm) for failure behavior of concrete. i: Theory." *Cement and Concrete Composites*, 33(9), 881–890.

Cusatis, G., Mencarelli, A., Pelessone, D., and Baylot, J. (2011a). "Lattice discrete particle model (ldpm) for failure behavior of concrete. ii: Calibration and validation." *Cement and Concrete composites*, 33(9), 891–905.

Cusatis, G. (2013). "The lattice discrete particle model (ldpm) for the numerical simulation of concrete behavior subject to penetration." *Materials under Extreme Loadings: Application to Penetration and Impact*, 369–387.

Cusatis, G. and Zhou, X. (2013). "High-order microplane theory for quasi-brittle materials with multiple characteristic lengths." *Journal of Engineering Mechanics*, 140(7), 04014046.

Cusatis, G., Rezakhani, R., and Schauffert, E. A. (2017). "Discontinuous cell method (dcm) for the simulation of cohesive fracture and fragmentation of continuous media." *Engineering Fracture Mechanics*, 170, 1–22.

De Schutter, G. and Taerwe, L. (1996). "Degree of hydration-based description of mechanical properties of early age concrete." *Materials and Structures*, 29(6), 335.

Di Luzio, G. and Cusatis, G. (2009a). "Hygro-thermo-chemical modeling of high performance concrete. i: Theory." *Cement and Concrete composites*, 31(5), 301–308.

Di Luzio, G. and Cusatis, G. (2009b). "Hygro-thermo-chemical modeling of high-performance concrete. ii: Numerical implementation, calibration, and validation." *Cement and Concrete composites*, 31(5), 309–324..

Di Luzio, G. and Cusatis, G. (2013). "Solidification–microprestress–microplane (smm) theory for concrete at early age: Theory, validation and application." *International Journal of Solids and Structures*, 50(6), 957–975.

Diamond, S., Chemistry and other characteristics of asr gels, in: Proceedings of the 11th International Conference on Alkali-Aggregate Reaction in Concrete, Quebec City, Canada, volume 31, p. 40.

Dormieux, L., Lemarchand, E., Kondo, D., and Fairbairn, E. (2004). "Elements of poro-micromechanics applied to concrete." *Materials and Structures*, 37(1), 31–42.

Dron, R., F. Brivot, Thermodynamic and kinetic approach to the alkali-silica reaction. part 1: Concepts, Cement and Concrete Research 22 (1992) 941–948.

Dron, R., F. Brivot, Thermodynamic and kinetic approach to the alkali-silica reaction. part 2: Experiment, Cement and Concrete Research 23 (1993) 93–103.

Fairbairn, M., Ribeiro, F., Toledo-Filho, R., Lopes, L., Silvoso, M., Aguas, M., and Guedes, Q. (2004). "Smeared cracking fem simulation of alkali-silica expansion using a new macroscopic coupled model." *Proceeding of the 12th International conference on Alkaliaggregate reaction in concrete ICAAR2004*, 104–114.

Farage, M., Alves, J., and Fairbairn, E. (2004). "Macroscopic model of concrete subjected to alkali–aggregate reaction." *Cement and Concrete Research*, 34(3), 495–505.

Fernandes, I., Composition of alkali–silica reaction products at different locations within concrete structures, Materials Characterization 60 (2009) 655–668.

Gallucci, E., Zhang, X., and Scrivener, K. (2013). "Effect of temperature on the microstructure of calcium silicate hydrate (csh)." *Cement and Concrete Research*, 53, 185–195.

Gawin, D., Pesavento, F., and Schrefler, B. A. (2006). "Hygro-thermo-chemo-mechanical modelling of concrete at early ages and beyond. part i: hydration and hygro-thermal phenomena." *International Journal for Numerical Methods in Engineering*, 67(3), 299–331.

Giaccio G., R. Zerbino, J. Ponce, O. R. Batic, Mechanical behavior of concretes damaged by alkali-silica reaction, Cement and Concrete Research 38 (2008) 993–1004.

Glasser, L. D., Osmotic pressure and the swelling of gels, Cement and Concrete Research 9 (1979) 515–517.

Glasser, L. D., N. Kataoka, The chemistry of alkali-aggregatereaction, Cement and Concrete Research 11 (1981) 1–9.

Grattan-Bellew, P., L. Mitchell, J. Margeson, D. Min, Is alkali–carbonate reaction just a variant of alkali–silica reaction acr= asr?, Cement and Concrete Research 40 (2010) 556–562.

Jensen, A. D., S. Chatterji, P. Christensen, N. Thaulow, H. Gudmundsson, Studies of alkali-silica reactionpart i a comparison of two accelerated test methods, Cement and Concrete Research 12 (1982) 641–647.

Jones, T., New interpretation of alkali-silica reaction and expansion mechanisms in concrete, Chemistry and industry (1988) 40–4.

Kagimoto, H., Y. Yasuda, M. Kawamura, Asr expansion, expansive pressure and cracking in concrete prisms under various degrees of restraint, Cement and Concrete Research 59 (2014) 1–15.

Katayama, T., Late-expansive asr in a 30-year old pc structure in eastern japan, in: Proc. 14th International Conference on Alkali-Aggregate Reaction (ICAAR), Austin, Texas, USA, paper.

Kawamura, M., K. Takemoto, N. Terashima, Effect of sodium chloride and sodium hydroxide from the surrounding solution on alkali-silica reaction in mortars containing fly ash, Magazine of Concrete Research 40 (1988) 143–151.

Kawamura, M., K. Iwahori, Asr gel composition and expansive pressure in mortars under restraint, Cement and concrete composites 26 (2004) 47–56.

Kim, T., J. Olek, Chemical sequence and kinetics of alkali-silica reaction part i. experiments, Journal of the American Ceramic Society 97 (2014) 2195–2203.

Larive, C., Apports combinés de l'expérimentation et de la modélisation à la compréhension de l'alcali-réaction et de ses effets mécaniques, Ph.D. thesis, Ecole nationale des ponts et chaussees, 1997.

Léger, P., Côté, P., and Tinawi, R. (1996). "Finite element analysis of concrete swelling due to alkali-aggregate reactions in dams." *Computers & structures*, 60(4), 601–611.

Lemarchand, E., Dormieux, L., and Ulm, F.-J. (2005). "Micromechanics investigation of expansive reactions in chemoelastic concrete." *Philosophical Transactions of the Royal Society of London A: Mathematical, Physical and Engineering Sciences*, 363(1836), 2581–2602.

Li, K. and Coussy, O. (2002). "Concrete asr degradation: from material modeling to structure assessment." *Concrete Science and Engineering*, 4(13), 35–46.

Lindgård, J., Ö. Andiç-Çakır, I. Fernandes, T. F. Rønning, M. D. Thomas, Alkali–silica reactions (asr): literature review on parameters influencing laboratory performance testing, Cement and Concrete Research 42 (2012) 223–243.

Louarn, N., C. Larive, Alcali-réaction et réaction sulfatique: synthèse des études microscopiques d'expertises de ponts dégradés, Bulletin de liaison des laboratoires des Ponts et Chaussées (1993).

Malla, S. and Wieland, M. (1999). "Analysis of an arch–gravity dam with a horizontal crack." *Computers & structures*, 72(1), 267–278.

Marzouk, H., S. Langdon, The effect of alkali-aggregate reactivity on the mechanical properties of high and normal strength concrete, Cement and Concrete Composites 25 (2003) 549–556.

Mirza, W. H., S. I. Al-Noury, W. H. Al-Bedawi, Temperature effect on strength of mortars and concrete containing blended cements, Cement and Concrete Composites 13 (1991) 197–202.

Monette, L., J. Gardner, P. Grattan-Bellew, Structural effects of the alkali-silica reaction on non-loaded and loaded reinforced concrete beams (2000).

Moon, Juhyuk, Speziale, Sergio, Meral, Cagla, Kalkan, Bora, Clark, Simon M, Monteiro, Paulo JM Determination of the elastic properties of amorphous materials: case study of alkali-silica reaction gel, Cement and Concrete Research 54 (2013) 55–60.

Multon, S., Evaluation expérimentale et théorique des effets mécaniques de l'alcali-réaction sur des structures modèles, Ph.D. thesis, Université de Marne-la-Vallée, 2003.

Na, O., Y. Xi, E. Ou, V. E. Saouma, The effects of alkali-silica reaction on the mechanical properties of concretes with three different types of reactive aggregate, Structural Concrete 17 (2016) 74–83.

Nixon, P. J., I. Sims, et al., Rilem recommended test method: Aar-0outline guide to the use of rilem methods in the assessment of the alkali-reactivity potential of aggregates, in: RILEM Recommendations for the Prevention of Damage by Alkali-Aggregate Reactions in New Concrete Structures, Springer, 2016, pp. 5–34.

Olafsson, H., The effect of relative humidity and temperature on alkali expansion of mortar bars, in: Proc., 7th Int. Conf. on Alkali Aggregate Reaction in Concrete, pp. 461–465.

Ono, K., Strength and stiffness of alkali-silica reaction concrete and concrete members, Structural Engineering Review 2 (1990) 121–125.

Pan, J., Y. Feng, J. Wang, Q. Sun, C. Zhang, D. Owen, Modeling of alkali-silica reaction in concrete: a review, Frontiers of Structural and Civil Engineering 6 (2012) 1–18.

Pan, Y., Prado, A., Porras, R., Hafez, O. M., and Bolander, J. E. (2017). "Lattice modeling of early-age behavior of structural concrete." *Materials*, 10(3), 231.

Pesavento, F., Gawin, D., Wyrzykowski, M., Schrefler, B. A., and Simoni, L. (2012). "Modeling alkali–silica reaction in non-isothermal, partially saturated cement based materials." *Computer Methods in Applied Mechanics and Engineering*, 225, 95–115.

Ponce, J., O. R. Batic, Different manifestations of the alkali-silica reaction in concrete according to the reaction kinetics of the reactive aggregate, Cement and Concrete Research 36 (2006) 1148–1156.

Poole, A. B., Alkali-silica reactivity mechanisms of gel formation and expansion, in: Proceedings of the 9th International Conference on Alkali-Aggregate Reaction, London (England), volume 104, Concrete Society Publications CS, pp. 782–789.

Prince, W., R. Perami, Mise en évidence du rôle essentiel des ions oh- dans les réactions alcali-silice, Cement and concrete research 23 (1993) 1121–1129.

Rahimi-Aghdam, S., Bažant, Z. P., and Caner, F. C. (2016). "Diffusion-controlled and creep-mitigated asr damage via microplane model. ii: Material degradation, drying, and verification." *Journal of Engineering Mechanics*, 143(2), 04016109.

Rezakhani, R. and Cusatis, G. (2016). "Asymptotic expansion homogenization of discrete fine-scale models with rotational degrees of freedom for the simulation of quasi-brittle materials." *Journal of the Mechanics and Physics of Solids*, 88, 320–345.

Saccani, A., V. Bonora, P. Monari, Laboratory short-term evaluation of asr: a contribution, Cement and concrete research 31 (2001) 739–742.

Šachlová, Š., R. Přikryl, Z. Pertold, Alkali-silica reaction products: Comparison between samples from concrete structures and laboratory test specimens, Materials Characterization 61 (2010) 1379–1393.

Sanchez, L., B. Fournier, M. Jolin, J. Duchesne, Reliable quantification of aar damage through assessment of the damage rating index (dri), Cement and Concrete Research 67 (2015) 74–92.

Saouma, V. and Perotti, L. (2006). "Constitutive model for alkali-aggregate reactions." *Materials Journal*, 103(3), 194–202.

Saouma, V. E., M. A. Hariri-Ardebili, A proposed aging management program for alkali silica reactions in a nuclear power plant, Nuclear Engineering and Design 277 (2014) 248–264.

Saouma, V. E., R. A. Martin, M. A. Hariri-Ardebili, T. Katayama, A mathematical model for the kinetics of the alkali–silica chemical reaction, Cement and Concrete Research 68 (2015) 184–195.

Schauffert, E. A. and Cusatis, G. (2011). "Lattice discrete particle model for fiber-reinforced concrete. i: Theory." *Journal of Engineering Mechanics*, 138(7), 826–833.

Schauffert, E. A., Cusatis, G., Pelessone, D., ODaniel, J. L., and Baylot, J. T. (2011). "Lattice discrete particle model for fiber-reinforced concrete. ii: tensile fracture and multiaxial loading behavior." *Journal of Engineering Mechanics*, 138(7), 834–841.

Sibbick, R., C. Page, Threshold alkali contents for expansion of concretes containing british aggregates, Cement and concrete research 22 (1992) 990–994.

Smaoui, N., M. Bérubé, B. Fournier, B. Bissonnette, B. Durand, Effects of alkali addition on the mechanical properties and durability of concrete, Cement and concrete research 35 (2005) 203–212.

Smith, J., Cusatis, G., Pelessone, D., Landis, E., O'Daniel, J., and Baylot, J. (2014). "Discrete modeling of ultra-high-performance concrete with application to projectile penetration." *International Journal of Impact Engineering*, 65, 13–32.

Stanton, T. E., Expansion of concrete through reaction between cement and aggregate, Proceedings of the American Society of Civil Engineers 66 (1940) 1781–1811.

Swamy, R., M. Al-Asali, Influence of alkali-silica reaction on the engineering properties of concrete, in: Alkalies in concrete, ASTM International, 1986.

Thaulow, N. , U. H. Jakobsen, B. Clark, Composition of alkali silica gel and ettringite in concrete railroad ties: Sem-edx and x-ray diffraction analyses, Cement and Concrete Research 26 (1996) 309–318.

Thomas, M. D., B. Fournier, K. J. Folliard, Alkali-aggregate reactivity (AAR) facts book, Technical Report, 2013.

Thompson, G., Charlwood, R., Steele, R., and Curtis, D. (1994). "Mactaquac generating station intake and spillway remedial measures." *Proceedings for the eighteenth international congress on large dams, Durban, South Africa*, Vol. 1, 347–68.

Ulm, F.-J. and Coussy, O. (1995). "Modeling of thermochemomechanical couplings of concrete at early ages." *Journal of engineering mechanics*, 121(7), 785–794.

Ulm, F.-J., Coussy, O., Kefei, L., and Larive, C. (2000). "Thermo-chemo-mechanics of asr expansion in concrete structures." *Journal of engineering mechanics*, 126(3), 233–242.

Wan, L., Wendner, R., Liang, B., and Cusatis, G. (2016). "Analysis of the behavior of ultra high performance concrete at early age." *Cement and Concrete Composites*, 74, 120–135.

Wang, H., J. Gillott, Effect of ca (oh) 2 on alkali–silica reaction, Magazine of Concrete Research 43 (1991a) 215–218.

Wang, H., J. Gillott, Mechanism of alkali-silica reaction and the significance of calcium hydroxide, Cement and Concrete Research 21 (1991b) 647–654.

Wendner, R., Nincevic, K., Boumakis, I., and Wan, L. (2016). "Age-dependent lattice discrete particle model for quasi-static simulations." *Key Engineering Materials*, Vol. 711, Trans Tech Publ, 1090–1097.

Wilson, M., J. Cabrera, Y. Zou, The process and mechanism of alkali silica reaction using fused silica as the reactive aggregate, Advances in Cement Research 6 (1994) 117–125.

Winnicki, A. and Pietruszczak, S. (2008). "On mechanical degradation of reinforced concrete affected by alkali-silica reaction." *Journal of engineering mechanics*, 134(8), 611–627.

Winnicki, A., Serega, S., and Norys, F. (2014). "Chemoplastic modelling of alkali-silica reaction (asr)." *Computational Modelling of Concrete Structures Euro-C 2014 Int. Conf*, 765–774.

Wu, T., Temizer, I., and Wriggers, P. (2014). "Multiscale hydro-thermo-chemo-mechanical coupling: Application to alkali–silica reaction." *Computational Materials Science*, 84, 381–395.

Grimal, E., Sellier, A., Multon, S., Pape, Y. L., and Bourdarot, E. (2010). "Concrete modelling for expertise of structures affected by alkali aggregate reaction." *Cement and Concrete Research*, 40(4), 502 – 507 Special Issue: ICAAR 13, Trondheim, Norway, June 16-20, 2008.

Multon, S. and Sellier, A. (2016). "Multi-scale analysis of alkalisilica reaction (asr): Impact of alkali leaching on scale effects affecting expansion tests." *Cement and Concrete Research*, 81(Supplement C), 122 – 133.

Kim, T., Olek, J., and Jeong, H. (2015). "Alkalisilica reaction: Kinetics of chemistry of pore solution and calcium hydroxide content in cementitious system." *Cement and Concrete Research*, 71(Supplement C), 36 – 45.

Prezzi, M., Monteiro, P. J., and Sposito, G. (1997). "The alkali–silica reaction: Part i. use of the double-layer theory to explain the behavior of reaction-product gels." *ACI materials journal*, 94(1), 10–17.

Pignatelli, R., Comi, C., and Monteiro, P. J. (2013). "A coupled mechanical and chemical damage model for concrete affected by alkalisilica reaction." *Cement and Concrete Research*, 53(Supplement C), 196 – 210.

Handbook, A. (1993). "Fundamentals. atlanta: American society of heating, refrigerating, and air-conditioning engineers.

Appendix

Hygro-Thermo-Chemical model equations:

(i) Based on a Fick's law, the moisture transport under isothermal conditions can be written as $\mathbf{J} = -D_h(h,T)\boldsymbol{\nabla} h$ where $\mathbf{J}$ is the flux of water mass per unit time and the moisture permeability has the following functional form $D_h(h,T) = D_1[1+(D_1/D_0-1)(1-h)^n]^{-1}\exp(E_{ad}/(RT_0) - E_{ad}/(RT))$. D_0, D_1 and n are material parameters, whereas T_0 is the reference room temperature, E_{ad} is the diffusivity activation energy and R is the universal gas constant. By writing the mass balance per unit volume of mortar, i.e. equating the rate of water content w to the divergence of the flux of water mass per unit time $\mathbf{J}$, and considering that the water content is divided in evaporable w_e and non-evaporable w_n water: $w = w_e + w_n$, on can obtain:

$$\boldsymbol{\nabla}\cdot(D_h\boldsymbol{\nabla} h) - \frac{\partial w_e}{\partial h}\frac{\partial h}{\partial t} - \frac{\partial w_e}{\partial \alpha_c}\dot{\alpha}_c - \dot{w}_n = 0 \tag{26}$$

(ii) The sorption/desorption isotherm defining the evaporable water as a function of relative humidity is introduced by distinguishing the evaporable water present in the C-S-H gel w_e^{gel} and in the capillary pores w_e^{cap}: $w_e = w_e^{gel} + w_e^{cap}$ through the following functional forms:

$$w_e^{gel} = k_{vg}^c \alpha_c c[1 - e^{-10(g_1\alpha_c^\infty - \alpha_c)h}] \tag{27}$$

$$w_e^{cap} = \frac{w_0 - 0.188\alpha_c c - k_{vg}^c\alpha_c c[1 - e^{-10(g_1\alpha_c^\infty-\alpha_c)}]}{[e^{10(g_1\alpha_c^\infty-\alpha_c)} - 1][e^{10(g_1\alpha_c^\infty-\alpha_c)h} - 1]^{-1}} \tag{28}$$

where c is the cement content, w_0 is the initial water content, k_{vg}^c and g_1 are material parameters. One can note that at saturation, $h = 1$, thus $w_e = w_0 - 0.188\alpha_c c$. This expression is further used when the ASR model will be introduced.

(iii) Concerning the temperature evolution, a Fourier's law is considered for the heat conduction $\mathbf{q} = -\lambda_T\boldsymbol{\nabla} T$ where $\mathbf{q}$ is the heat flux, and λ_T is the heat conductivity (defined for $T < 100°$C). By considering the rate of heat of hydration reaction generated per unit volume $\dot{Q}_c$ as a linear function of the rate of the degree of hydration $\dot{\alpha}_c$, one can write the enthalpy balance equation as:

$$\boldsymbol{\nabla}\cdot(\lambda_T\boldsymbol{\nabla} T) - \rho c_T\frac{\partial T}{\partial t} + \dot{\alpha}_c c\tilde{Q}_c^\infty = 0 \tag{29}$$

where $\tilde{Q}_c^\infty$ is the latent heat of hydration reaction per unit of hydrated mass, assumed constant for a given mortar, ρ and c_T are respectively the density and the isobaric heat capacity of mortar.

Table 5. Parameters governing the hygro-thermo-chemical modeling.

Par.	Units	Value	Description	Calibration test	Source
c_T^{cal}	J kg^{-1} K^{-1}	1680	Heat capacity of rubber	Thermal conductivity	(a)
ρ^{cal}	kg m^{-3}	72	Density of rubber	Density	(a)
λ_T^{cal}	W m^{-1} K^{-1}	6.6×10^{-2}	Heat conductivity of rubber	Thermal conductivity	Idf
c_T	J kg^{-1} K^{-1}	1100	Heat capacity of mortar	Thermal conductivity	(b)
ρ	kg m^{-3}	2591	Density of mortar	Density	Idf
λ_T	W m^{-1} K^{-1}	2.3	Heat conductivity of mortar	Thermal conductivity	(b)
A_{c1}	h^{-1}	6×10^{7}	Cement hydration par.	Calorimetric	Idf
A_{c2}	-	7×10^{-3}	Cement hydration par.	Calorimetric	Idf
η_c	-	6.5	Cement hydration par.	Calorimetric	Idf
E_{ac}	J mole^{-1}	45646	Hydration activation energy	Reaction rate	(b)
$\tilde{Q}_c^{\infty}$	J kg^{-1}	520×10^{3}	Cement hydration enthalpy	Calorimetric	(b)
D_0	kg m^{-1} h^{-1}	1.9×10^{-6}	Permeability par.	Drying	(b)
D_1	kg m^{-1} h^{-1}	2.5×10^{-3}	Permeability par.	Drying	(b)
n	-	3.25	Permeability par.	Drying	(b)
E_{ad}	J mole^{-1}	22449	Diffusivity activation energy	Drying	(b)
k_{vg}^c	-	0.2	Evaporable water in CSH gel	Isotherms	(b)
g_1	-	1.5	Evaporable water in capillaries	Isotherms	(b)

Par.: Parameter, Idf.: Identified, (a) Handbook (1993), (b) Di Luzio and Cusatis (2009b).

Table 6. Parameters governing the mechanical behavior and aging modeling.

Par.	Units	Value	Description	Calibration test	Source
A_λ	-	0.5	Aging material par.	Elastic modulus data	Idf
α_0	-	0.15	Hydration degree at setting	Vicat or Gillmore needle	(b)
n_λ	-	0.65	Aging material par.	Elastic modulus data	Idf
n_a	-	1.17	Aging material par.	Comp. and fracture	Idf
m_a	-	1.5	Aging material par.	Comp.	Idf
k_a	-	3.58	Aging material par.	Fracture	Idf
E_0^∞	GPa	66.5	Asp. normal modulus	Fracture	Idf
α	-	0.25	Poisson's effect par.	Comp. or tension	(c)
σ_t^∞	MPa	9.53	Asp. mesoscale tensile strength	Fracture	Idf
r_{st}^∞	MPa	9.53	Asp. mesoscale shear strength ratio	Comp.	Idf
l_t^∞	mm	31.92	Asp. characteristic length	Fracture	Idf
μ_0	-	0.2	Frictional behavior par.	Triaxial comp. at l.c.	(c)
σ_{N0}	MPa	500	Frictional behavior par.	Triaxial comp. at h.c.	(c)
σ_{c0}	MPa	123	Yielding and pore collapse par.	Hydrostatic comp.	(c)
H_{c0}/E_0	-	0.4	Yielding and pore collapse par.	Hydrostatic comp.	(c)
H_{c1}/E_0	-	0.1	Yielding and pore distortion par.	Passively confined	(c)
κ_{c0}	-	2	Dens. after pore distortion par.	Hydrostatic comp.	(c)
κ_{c1}	-	1	Dens. after pore distortion par.	Hydrostatic comp.	(c)
κ_{c2}	-	5	Dens. after pore distortion par.	Hydrostatic comp.	(c)
κ_{c3}	-	0.1	Dens. after pore distortion par.	Hydrostatic comp.	(c)

Asp.: Asymptotic, l.c.: low confinement, h.c.: high confinement, comp.: compression, Dens.: Densification, (b) Di Luzio and Cusatis (2009b). (c) Cusatis et al. (2011b).

Table 7. Parameters governing the alkali silica reaction modeling.

Par.	Units	Value	Description	Calibration test	Source
ρ_g	kg m^{-3}	252.77	ASR gel density	Free exp.	(d)
k_z	cm^5 kg^{-1} day^{-1}	8.04	ASR gel formation par.	Free exp.	Idf
k_i	-	0.12	Water imbibition par.	Free exp.	Idf
$\tilde{C}_i$	mm^2 day^{-1}	0.69	Water imbibition par.	Free exp.	Idf
δ_c	mm	0.0052	ITZ porosity effect par.	Free exp.	Idf
c_{a0}	kg m^{-3}	2.7	a.c. effect par.	Free exp. and different a.c.	(d)
c_{a1}	kg m^{-3}	4.37	a.c. effect par.	Free exp. and different a.c.	(d)
κ_a	-	1	a.c. effect par.	Free exp. and different a.c.	(d)

Free exp.: Free ASR expansion test at 100% relative humidity, a.c.: alkali content, (d) (Alnaggar et al., 2013)